Ricardo Sérgio Gomes Almeida Loução

Bachelor of Science

Structural Connectivity based on Diffusion Kurtosis Imaging

Dissertation submitted in partial fulfilment
of the requirements for the degree of

Master of Science in
Biomedical Engineering

Adviser: Hugo Alexandre Ferreira, Auxiliary Professor,
Faculty of Sciences of University of Lisbon

Co-adviser: Rita G. Nunes, Auxiliary Investigator,
Faculty of Sciences of University of Lisbon

FACULDADE DE
CIÊNCIAS E TECNOLOGIA
UNIVERSIDADE NOVA DE LISBOA

September, 2015

Structural Connectivity based on Diffusion Kurtosis Imaging

This document was created unsing the (pdf)LaTeX processor, based in the "unlthesis" template[1], developed at the Dep. Informática of FCT-NOVA [2]. [1] https://github.com/joaomlourenco/unlthesis [2] http://www.di.fct.unl.pt

À minha mãe, por todas as oportunidades que não me foram negadas, e aos meus irmãos, para que se inspirem a chegar mais longe ainda.

Acknowledgements

Funny that this is the first piece of text in this document, and yet was the last one to be written...

This was, by far, the hardest task I've ever set myself to do (come to think of it, I was actually told to do this, but I just wanted to add drama to the text). Writing this dissertation often drew me out of my strength and it was through the support of friends and family that I kept on going. This chapter is dedicated to them.

First and foremost, my advisor and co-advisor, Prof. Hugo Ferreira and Prof. Rita Nunes (to whom I've already been granted permission to address to simply as Rita - a great accomplishment!). Without them none of this was possible. No thesis plan, obviously, but more importantly, no lengthy, yet highly productive, meetings discussing the paths to take and the results obtained, while still maintaining the casual register, always making me feel at easy in their presence. To them I would like to express my greatest gratitude, not only for the time wasted with me but also for the high degree of patience displayed. Prof. Hugo, please note that I did not forget we still have a bottle of Oporto wine to finish and a tandem jump to do!

Still on an academic note, I would like to thank my overseas counsellors, Marta Correia, Rafael Neto-Henriques and André Ribeiro. Each in their own field of expertise, provided me with invaluable tips and information, which without them, this dissertation would be seriously undermined.

On a more personal note, thanks are due to my faculty buddies, Ameixa, Mota, Juliana (aka Júlia), Rito, Ana Carolina (aka Fradinho), Flávio (aka Prof. Rocha), Débora (here's your paragraph!!) and Soraia, for forcing me to laugh in times of utter despair and for forcing me to make them laugh in their time of despair, increasing the overall happiness in the world. Furthermore, I would like to thank them for all of the parties attended together, all of the nights where sorrows were drowned and hangovers that followed suit!

Carrying on with the personal thank you note, throughout my academic years I have established special connections with special people with whom I have the pleasure to share a very special bond. To Lina, Jéssica, Dalila, Idalizia, Ana Leonor, Franga and Swag (and Onofre!), thanks for all of the coffees we've had together, all of the smiles that brightened my day and just everything you did for me/with me.

E este será o único parágrafo escrito em Português (à parte do resumo obviamente), porque as pessoas que nele vêm mencionadas merecem um tratamento diferente. Aos

meus irmãos quero agradecer por todos os dias esticarem o meu limite de paciência (que me ajudou imenso [!!!] a lidar com as múltiplas personagens que fui conhecendo) e por estarem sempre dispostos a alinhar nas minhas baboseiras, por mais parvas que elas sejam, fruto de um longo dia de tese. E, finalmente, à pessoa que realmente tornou isto possível, à minha mãe. Sem a qual não teria nascido, e consequentemente não teria atingido esta grande meta da minha vida (entre muitas outras coisas, que não há espaço para dizer e por isso ficarão para outra altura). A vós este documento.

Abstract

Structural connectivity models based on Diffusion Tensor Imaging (DTI) are strongly affected by the technique's inability to resolve crossing fibres, either intra- or inter-hemispherical connections. Several models have been proposed to address this issue, including an algorithm aiming to resolve crossing fibres which is based on Diffusion Kurtosis Imaging (DKI). This technique is clinically feasible, even when multi-band acquisitions are not available, and compatible with multi-shell acquisition schemes. DKI is an extension of DTI enabling the estimation of diffusion tensor and diffusion kurtosis metrics. In this study we compare the performance of DKI and DTI in performing structural brain connectivity.

Six healthy subjects were recruited, aged between 25 and 35 (three females). The MRI experiments were performed using a 3T Siemens Trio with a 32-channel head coil. The scans included a T1-weighted sequence ($1mm^3$), and a DWI with b-values 0, 1000 and 2000 $s.mm^{-2}$. For each b-value, 64 equally spaced gradient directions were sampled. For DTI fitting only images with b-value of 0 and 1000 $s.mm^{-2}$ were considered, whereas for the DKI fitting, the whole cohort of images were considered. To fit both DTI and DKI tensors, extract the metrics and perform tract reconstructions, the toolbox DKIu was used, and the structural connectivity analysis was accomplished using the MIBCA toolbox.

Tractography results revealed, as expected, that DKI-based tractography models can resolve crossing fibres within the same voxel, which posed a limitation to the DTI-based tractography models. Structural connectivity analysis showed DKI-based networks' ability to establish both more inter-hemisphere and intra-hemisphere connections, when compared to DTI-based networks. This may be a direct consequence of the inability to resolve crossing fibres when using the DTI model. The DKI model ability to resolve crossing fibres may provide increased sensitivity to both inter- and intra-hemispherical connections.

DTI-based modularity connectograms show a distinct intra-hemispherical configuration, whereas DKI-based connectograms show an increased number of inter-hemispherical connections, with several clusters extending over both hemispheres. Global and local connectivity metrics were also studied, but yielded no conclusive results. This may be due to a lack of reproducibility of the metrics or of the small cohort of subjects considered.

DKI seems to provide additional insights into structural brain connectivity by resolving crossing fibres, otherwise undetected by DTI.

Keywords: Diffusion Tensor Imaging, Diffusion Kurtosis Imaging, Tractography, Structural Connectivity

Resumo

Modelos de conectividade estrutural baseados em Imagem por Tensor de Difusão (DTI) são fortemente afetados pela limitação da técnica em resolver cruzamentos de fibras intra-voxel, quer a um nível de ligações intra-hemisféricas ou inter-hemisféricas. Vários modelos têm sido propostos para tentar colmatar este problema, incluindo um algoritmo focado para a resolução destes cruzamentos de fibras baseado em Imagem por Curtose de Difusão (DKI). Esta técnica é clinicamente exequível, mesmo quando esquemas de aquisição *multi-band* não estão disponíveis. DKI funciona como uma extensão do DTI, na medida em que permite estimar métricas do tensor de difusão assim como do tensor de curtose. Neste estudo comparamos o desempenho do DKI e do DTI em conectividade estrutural do cérebro.

Seis sujeitos saudáveis foram recrutados, com idades compreendidas entre os 25 e 35 anos (três de sexo feminino). As aquisições de Ressonância Magnética (IRM) foram executadas utilizando um aparelho 3T Siemens Trio com uma bobina de receção de 32 canais. As aquisições incluíram uma sequência ponderada em T1 ($1 mm^3$), e DWI com valores de b de 0, 1000 e 2000 $s.mm^{-2}$. Para cada valor de b, 64 direções de gradiente igualmente espaçadas foram adquiridas. Para estimar o tensor de DTI foram apenas consideradas imagens com valor de b igual a 0 e 1000 $s.mm^{-2}$, mas para estimar o tensor DKI, foram utilizadas todas a imagens adquiridas. Para estimar os tensores de difusão e curtose, extrair as métricas e realizar a reconstrução por tractografia, foi utilizado o programa DKIu, e para a análise da conetividade estrutural foi utilizada a toolbox MIBCA.

Os resultados das tractografias revelaram, como esperado, que os tractos estimados com base em algoritmos de DKI conseguem resolver cruzamento de fibras dentro do mesmo voxel, que é uma limitação da abordagem por DTI. A análise da conectividade estrutural revelou resultados interessantes no que toca à capacidade das redes computadas por DKI reonhecerem mais ligações quer inter-hemisféricas quer intra-hemisféricas, quando comparadas com as redes computadas por DTI. Isto pode ser uma consequência directa da incapacidade de resolução de cruzamento de fibras quando se utiliza o modelo de DTI. A resolução de fibras cruzadas pelo modelo DKI pode providenciar uma sensibilidade acrescida a ligações quer inter-hemisféricas quer intra-hemisféricas.

Conectogramas de modularidade baseados em DTI mostram uma clara configuração intra-hemisférica de agrupamentos, ao passo que conectogramas baseados em DKI

mostram agrupamentos que englobam ambos os hemisférios, com múltiplas ligações inter-hemisféricas dentro do mesmo agrupamento.

As métricas de conectividade globais e locais também foram estudadas, mas parecem sofrer de grande variabilidade, pelo que os resultados foram inconclusivos. Esta variabilidade pode dever-se a falta de reprodutibilidade das métricas estudadas ou do número de sujeitos considerados ter sido baixo.

DKI parece fornecer nova informação para a conectividade estrutural do cérebro ao resolver cruzamento de fibras, mas a verdadeira extensão dessa melhoria ainda está em estudo.

Palavras-chave: Imagem por Tensor de Difusão, Imagem por curtose de difusão, Tractografia, Conectividade Estrutural

Contents

List of Figures

List of Tables

Acronyms

AD Axial Diffusivity.

ADC Apparent Diffusion Coefficient.

AK Axial Kurtosis.

aMRI anatomical MRI.

BCT Brain Connectivity Toolbox.

BET Brain Extraction Tool.

CC Corpus Callosum.

CLS Constrained Least Square.

CLS-KT Constrained Least Squares fitted Kurtosis Tensor.

CST Cortico-Spinal Tracts.

DKI Diffusion Kurtosis Imaging.

dODF diffusion Orientation Distribution Function.

dPDF diffusion displacement Probability Density Function.

DSI Diffusion Spectrum Imaging.

DT Diffusion Tensor.

DTI Diffusion Tensor Imaging.

DWI Diffusion Weighted Imaging.

FA Fractional Anisotropy.

FA$_K$ Kurtosis Fractional Anisotropy.

FID Free Induction Decay.

FSL FMRIB Software Library.

HARDI High Angular Resolution Diffusion Imaging.

IC Internal Capsule.

KT Kurtosis Tensor.

L-DT Linearly fitted Diffusion Tensor.

MD Mean Diffusivity.

MDD Main Diffusivity Direction.

MIBCA Multimodal Imaging Brain Complexity Analysis.

MK Mean Kurtosis.

MRI Magnetic Resonance Imaging.

nL-DT Non-Linearly fitted Diffusion Tensor.

OLS Ordinary Least Square.

OLS-KT Ordinary Least Squares fitted Kurtosis Tensor.

PGSE Pulsed Gradient Spin Echo.

RD Radial Diffusivity.

RF Radio Frequency.

RK Radial Kurtosis.

ROI Region of Interest.

SPM Statistical Parametric Mapping.

SS-EPI Single Shot Echo Planar Imaging.

TRSE Twice Refocused Spin Echo.

uDKI United Diffusion Kurtosis Imaging.

WM White Matter.

Chapter 1

Introduction

1.1 Context and Motivation

Diffusion Weighted Imaging (DWI), a kind of Magnetic Resonance Imaging (MRI) sensitive to diffusion, has been continuously evolving since its introduction, in the mid-1980's, proving its worth against the other techniques used to inspect the human body in a non-invasive way. Based on the principle of diffusion observed in water molecules, DWI has been particularly relevant in the study of regions where diffusion motion tends to be anisotropic. This is the case of white matter fibres in the brain. Such behaviour helps to understand the organization and connections of the structures in soft tissues at a macro-scale. Hence, the study of the whole brain's structural connectivity can be performed using the information provided by DWI techniques.

In its early days, DWI were modelled describing water diffusion as a scalar, in order to assess whether the diffusion was higher (brighter voxels) or lower (darker voxels) in a particular region. But this description was found to be very limited and there was the need to characterize and not only quantify diffusion but also its three-dimensional orientation. Diffusion Tensor Imaging (DTI) was then introduced. In its foundation lies the assumption that water diffusion can be approximated by a Gaussian model, and that a full characterization of the water diffusion can be accomplished estimating a diffusion tensor. This lead to a revolution in the imaging world, allowing the first *in vivo* visualization of brain fibres, through means of tractography, and numerous breakthroughs in the perception of structural modifications due to pathological conditions.

However, this technique has a few shortcomings when trying to study connectivity. DTI assumes that, for a single voxel, there is only one fibre population. This is generally the case in the brain, but it has been estimated that more than 30% of the voxels in a standard resolution brain image have, at least, two different fibre populations, travelling

in two distinct directions, crossing each other. Using the DTI model, voxels with multiple fibres are assigned lower fractional anisotropy (anisotropy intrinsic to each voxel) than the real one, due to the contributions of multiple fibres, lowering the overall anisotropy for that voxel. In addition to that, the overall Main Diffusivity Direction (MDD) for that voxel is also affected. This introduces both false positives and false negatives tract connections in DTI-based tractography reconstruction. Furthermore, the Gaussian model seems to be a poor fit to the biological diffusion scenario. The high complexity of the structures at hand (myelin sheaths, cellular organelles, etc.) have been shown to result in water molecular diffusion to look more like a sharper and thinner version of the Gaussian distribution. Thus, using a Gaussian model to characterize diffusion in biological tissues is often inaccurate.

To help mitigate these limitations, a new set of techniques have been developed, such as Diffusion Spectrum Imaging (DSI) and High Angular Resolution Diffusion Imaging (HARDI). These techniques offered improvements on the DTI flaws, particularly in solving the tractography-related limitations, acquiring images with multiple shells. These multi-shell acquisition schemes enable the description of the full diffusion function using measurements such as displacement, zero-probability and kurtosis. But this extra sensitivity comes with a hefty cost: lengthy acquisition times. This completely rules out the implementation of these techniques in a clinical environment.

Diffusion Kurtosis Imaging (DKI) was also developed to deal with the limitations of DTI. Working with a lower range of b-values than the previous techniques, DKI is both clinically feasible and allows for multi-shell acquisition schemes. DKI also abandons the Gaussian model, extending it to include a kurtosis dependent term, which is a statistical measurement that determines the degree of deviation of a distribution from a Gaussian distribution. In addition to estimating all DTI-derived metrics, DKI modelling also allows estimating kurtosis derived metrics, which can better characterize the spatial architecture of tissue microstructure. Therefore, the DKI model acts as an extension of the DTI model.

These improved methods lead to the growing interest in studying the brain's connectivity *in vivo* and non-invasively. Tractography reconstructions produce large datasets of anatomical connections patterns, and to better analyse these patterns, they are often represented as complex networks. Brain networks comprise nodes (vertices) and links (edges), and the network's inherent metrics can be very useful to understand the structural organization of the brain, both locally and as a whole.

Therefore, improvements in imaging techniques may reveal important pieces of information otherwise omitted. Information like this may lead to a more accurate reconstruction of the brain fibres, making the end result a more robust tractography, and, consequently, a better characterization of the brain's structural connectivity.

1.2 Objectives and Dissertation Plan

This dissertation has two primary objectives:

- Compare the performances of DTI and DKI-based tractographies, particularly in resolving intra-voxel crossing fibres.
- Compare network metrics, both local and global, characterizing DTI and DKI networks.

To do so, the present dissertation has been structured so as to first cover the current state-of-the-art concerning structural connectivity and DKI. Afterwards, the reader will be given a comprehensive explanation of the relevant theoretic underpinnings of diffusion MRI, such as acquisition schemes and formulations; tractography, what is it and how is it performed; and connectivity, from networks to biological inferences. Secondly, the reader will be introduced to the methods and materials used to perform this study, datasets used, image processing steps and statistical analysis. Thirdly, the results will be presented to the reader, according to each study, as well as their discussion. Finally, the conclusion and future work chapter will summarize the dissertation's findings and inform the reader on potential paths to take in future endeavours.

1.3 State-of-the-Art

The brain has been a subject of study ever since there was a need to understand how it worked. Primal research methods were performed *ex-vivo*, during autopsies, since there was no other way to inspect the human brain without compromising its integrity. Later, with the development of imaging technologies, research evolved into the *in vivo* methods we have today, such as MRI [1]. White matter has been focus of study many times [2, 3, 4, 5], particularly because it plays a key role in the brain's structure and function.

Through the modification of MRI acquisition schemes, it is possible to sensitize MRI to the random motion of water, or diffusion. Since water diffusion is bounded by cellular structures, which in the brain's case are myelin sheaths, it is possible to relate the water diffusion to the microstructures that limit it. The development of diffusion sensitive MRI techniques brought upon an increase in the brain structure studies, which are based on fibre tract reconstruction, or tractography [6, 7, 8, 9, 10, 11]. Tractography reconstruction is based on the grounds that water diffusion in the brain is conditioned by axons and their myelin sheats, and thus the water molecules show a preferred direction of diffusion (along the fibres rather than across). This is then used to assess inter-voxel connectivity based on the preferred direction of diffusion. All of this makes diffusion weighted MRI a prime tool to assess, in a non-invasive way, the direction of fibres in white matter and, consequently, brain connectivity.

DTI was the first technique to be used to extract information on the characterization of the white matter fibres for fibre tracking [6, 7]. A diffusion tensor was fitted to the diffusion distribution assuming that the displacement function of the molecules in the axons is Gaussian. Information on the brain's microstructures is then inferred and has been used in a wide variety of neurosciences, from the basic neuroscience [12] to diagnostic

neuroradiology [13]. But it showed several limitations, like diffusion not being Gaussian in biological tissues and lack of sensitivity to crossing fibres inside the same voxel [14, 15]. To mitigate these limitations, two approaches were used: whether to use different imaging models, from model free approaches like Q-Ball Imaging [16], Diffusion Spectrum Imaging [17] or Hybrid Diffusion Imaging [18], to modelled approaches like DKI [19]; or to use new and refined tractography algorithms, such as Spherical Deconvolution [20] or High Angular Resolution Diffusion Imaging [8], and also expanding on the deterministic (conventional) tractography to probabilistic [21] and global [22] algorithms.

Studies have been carried out comparing the performance of the tractography algorithms, on synthetic cases [23] and on real data [24], and global tractography seems to provide with better results, followed by probabilistic and then by deterministic. In the deterministic algorithms, single compartmental models (like DTI) are out-performed by any other of the above mentioned, due to the lack of sensitivity to the crossing fibres. Despite their optimistic results, both global and probabilistic tractography algorithms are computationally very time consuming [25], which rules them out for uses outside research, at least until computational advances are reached to meet the clinical time demands. Deterministic tractography computation times are shorter and therefore offer a better trade off between results and computation time. As for the the model free diffusion models, all of these techniques show better results with multiple and high b-values [16, 26], resulting in lengthy acquisition schemes. In turn, this also becomes a big limitation to their use in the clinical scope.

The recent introduction of DKI has provided the medical and scientific community with more tools to evaluate axonal and myelin integrity in white matter regions [19], at clinically feasible times while maintaining the multi-shell acquisitions (multiple b-values). In fact, recent studies reveal that DKI information can be of more value than that of DTI, either from a microstructural point of view [27, 28, 29] or from a connectivity stand point [30, 31]. It was further introduced by Rudrapatna et. al [32] the notion that DKI could present both complementary and exclusive information, proposing that DKI not only provides unique information but increased sensibility to the microsctructures of white matter. DKI then proves itself to be an advantageous method for studying the structural organization and connectivity of healthy white matter [33], and to assess structural modifications linked to pathological cases [34]. Furthermore, DKI is able to successfully address the crossing fibres problem, brought upon by the DTI model. This increased sensitivity may yield additional insights when it comes to whole brain connectivity.

Studies encompassing both DKI and connectivity are yet few in numbers, with only a few studies assessing human brain asymmetric connectivity based on DKI [30], with studies of whole brain connectivity still non-existent. It is therefore important to fill in this gap in the research, and determine whether or not DKI-based whole brain connectivity yields any assets beyond those of DTI-based connectivity.

1.4 Dissertation outputs

Throughout the development of this dissertation, several pieces of work were performed, either part of the main project or as side-projects, that produced some type of output. As part of the main project, the following works have resulted:

Publications

- Loução, R.; Nunes, R.G.; Neto-Henriques, R.; Correia, M. M.; Ferreira, H. A., "Human brain tractography: A DTI vs DKI comparison analysis", 2015 IEEE 4th Portuguese Meeting on Bioengineering (ENBENG) proceedings, pp.43-44, 26-28 Feb. 2015

Communications

- Loucao, R.; Nunes, R.G.; Neto-Henriques, R.; Correia, M.; Santos-Ribeiro, A., Ferreira, H.A., "Structural Connectivity Based on Diffusion Kurtosis Imaging" accepted to ESMRMB, 1-3 October 2015, Edinburgh, Scotland
- R. Loução, R. G. Nunes, R. Neto-Henriques, M. M. Correia, H. A. Ferreira, "Human brain tractography: a DTI vs DKI comparison analysis", 4th Portuguese BioEngineering Meeting, 26-28 February 2015, Porto, Portugal.
- A. Santos-Ribeiro, L. M. Lacerda, R. Neto-henriques, R. Maximiano, R. Loução, D. Nutt, J. McGonigle, H. A. Ferreira, "MIBCA, A toolbox for processing and analysis of multimodal imaging and connectivity data", 2015 International Conference on Brain Informatics & Health, 30 Aug - 2 Sept 2015, London, UK

As a side-project, a 3D tractography visualizer was developed in Unity. The final result will incorporate the Unity environment, the Leap Motion and Oculus Rift, to make an immersive 3D visualizer of tractography, controlled solely by the Leap Motion sensor. Another side-project was the study of the effect of downsampling the amount of b-vectors towards the minimum amount required to estimate the kurtosis tensor (see 2.3.1), as part of an ERASMUS internship project. From this project, it was determined that only kurtosis tensor related metrics (see 2.3.1) are affected by the downsampling, whereas the diffusion tensor based metrics (see 2.2.1) remained unchanged. These projects were not includes in the present dissertation since they involved no connectivity studies, putting them outside the scope of the dissertation.

Chapter 2

Theoretic Underpinnings

In this chapter, the reader will be introduced to all of the theoretic concepts needed to understand the content of the remaining chapters of this dissertation. First, an overview on MRI and how it can be sensitized to water diffusion in biological tissues. Then, more in depth, the two methods of DWI used in this work will be explained, DTI and DKI, from their formulation to advantages and pitfalls. Moving on, the tractography section will inform the reader on how these reconstructions are performed, based on the diffusion and kurtosis tensors. Finally, an overview on connectivity will be presented, describing what it is and why it is used in this context, while also introducing connectivity metrics and their biological interpretation.

2.1 Diffusion and MRI

2.1.1 Physics of MRI

MRI is a non-invasive diagnosis technique used to provide anatomical images of the human body, usually with a high spatial resolution and soft tissue contrast. To do so, MRI focuses on the atomic nuclei magnetic properties, in particular, those of the hydrogen nucleus. A hydrogen nucleus is composed by a proton which precesses around itself, described by the angular momentum of the nucleus, called spin. Other nuclei could be considered, but the hydrogen nucleus is the preferred one due to its abundance in water and fat, two main elements of the human body.

In the absence of an external magnetic field, the protons precess around random directions, and the net value of the magnetization of the whole cohort is, therefore, null.

When exposed to a strong magnetic field, the protons are forced to align in the direction parallel or antiparallel to that of the field and precess around it. These two directions of alignment are a consequence of the existence of two energy levels that the protons can

occupy inside the magnetic field. Since one level has a slightly lower energy than the other, the lower energy level will have more protons than the higher energy level; this difference causes the net magnetization to be different from zero. To this magnetic component we call longitudinal magnetization (M_0).

The frequency at which protons precess when immersed in the magnetic field is given by

$$\omega_0 = \gamma B_0 \tag{2.1}$$

where ω_0 is the Larmor frequency, γ is the gyromagnetic ratio of the atom and B_0 is the intensity of the magnetic field. In order to acquire signal, a disruption has to be made in the system. So, Radio Frequency (RF) pulses are applied in a direction perpendicular to that of B_0, creating a new magnetic component called transverse magnetization (M_{xy}). The RF pulse must be applied at the Larmor frequency so as to induce resonance. This forces the spins to precess at a given angle from the original magnetic field on the xy plane (provided we consider z as the axis longitudinal to B_0), and this angle depends on the pulse's characteristics (duration and intensity). Finally, when the RF pulse is switched off, the spins relax into the main direction again. Since these processes take time to occur, and the time taken is intrinsic to each tissue, it is possible to establish a correspondence between tissue type and the signal acquired. There are two different relaxation times to be considered. T1, or spin-lattice relaxation time, is the time taken for 63% of M_0 to recover after a 90°RF pulse. T2, or spin-spin relaxation time, corresponds to the time it takes for 37% of M_{xy} to be obtained due to relaxation of transverse magnetization, from a given value, determined by the RF pulse duration and intensity (see Figure 2.1). T2 is influenced also by interactions between spins, and if the inherent field inhomogeneities

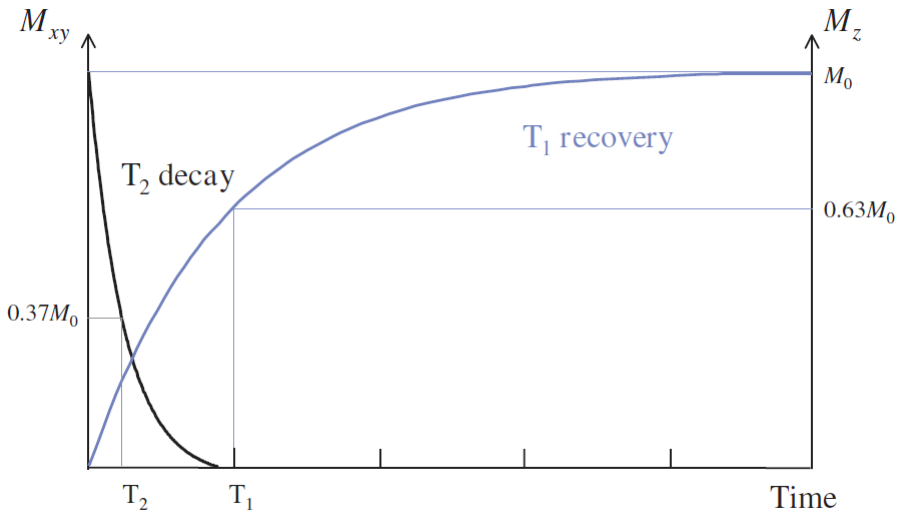

Figure 2.1: T1 and T2 relaxation times [35]. Although they happen at the same time, T2 is much smaller than T1.

are also considered, the relaxation will occur at a rate of T2* instead, which is shorter than T2.

The variation of M_{xy} is then detected by a receiving coil, in which, by induction, an electric current is generated. The decay of this current is exponential with the relaxation. The signal obtained in the coil is called Free Induction Decay (FID).

2.1.2 Diffusion Weighted Imaging

Diffusion, or brownian motion, is the random displacement of particles in a fluid. This displacent can be characterized by the diffusion constant. At a constant temperature, the diffusion constant D is given by Einstein's equation [36]

$$D = \frac{\overline{R}^2}{6t} \tag{2.2}$$

where $\overline{R}^2$ is the mean square displacement of the particles and t the time interval during which the displacement occurred.

In an unbounded environment, the water diffusion is the same in all directions in a given amount of time. This kind of diffusion is called isotropic diffusion. However, the same does not apply in the human body. Due to the presence of cell membranes and other cellular structures, water molecules are conditioned in their diffusion. This means that water molecules are allowed to travel longer distances in some directions that in others, for the same time interval. This phenomenon is called anisotropic diffusion.

In the brain's White Matter (WM), the water in the axons is restricted by the myelin sheath and cell membrane, constituting barriers to free diffusion. This, in turn, means that the diffusion will be more prominent along the direction parallel to the axis of the axons. This assumption is particularly important when studying the WM microstructure.

DWI is an imaging technique that is sensitive to water diffusion. When it first appeared, diffusion was modelled using a simple scalar, coded by pixel brightness. Then, with the appearance of DTI, a full three dimensional characterization became possible. In either case, diffusion is measured through the Apparent Diffusion Coefficient (ADC). The term *apparent* is used in *in vivo* acquisitions because it is impossible to differentiate diffusion from other sources of water mobility. ADC values depend on the motion-probing gradients and on their time interval. It takes any value from 0, if no motion is present, to the diffusion coefficient D, if diffusion is the only water motion phenomenon present [37].

2.1.3 Imaging Sequences

In order to acquire a DWI signal, a number of imaging sequences are available. Of those, only the ones relevant to the understanding of this dissertation will be presented.

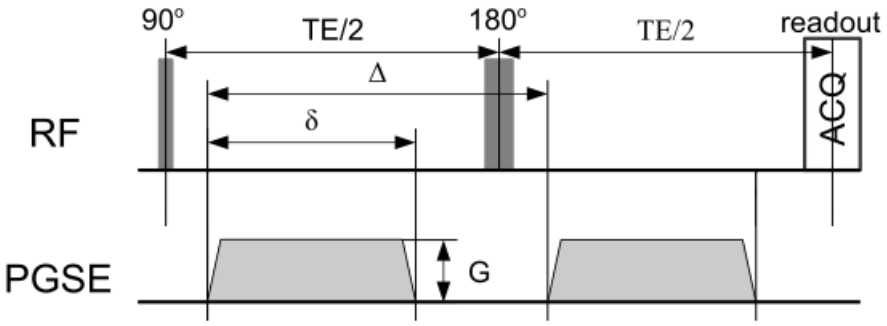

Figure 2.2: PGSE sequence scheme. Adapted from [39].

2.1.3.1 Pulsed Gradient Spin Echo

One of the most used acquisition schemes is called Pulsed Gradient Spin Echo (PGSE). Created by Stejskal and Tanner, it consists of two RF pulses, one of 90º and the second of 180º, and two magnetic gradients, with intensity G and time span δ, before and after the 180º RF pulse[38], as seen in 2.2.

The first gradient offsets the phase of the water protons' spins by a certain angle, and the second one resets the phase by the same angle. However, between the application of these gradients, spins randomly lose coherence due to diffusion. This means that the final phase of the spin will not be the same, resulting in an attenuation of the signal. This difference is the result of water diffusion, measured as the ADC.

Since diffusion in MRI acquisitions is represented as a signal decay, quantifying diffusion can be achieved using a scalar D and the signal obtained can be described by:

$$S(b) = S_0^{-bD} \tag{2.3}$$

where D is the diffusion coefficient, S_0 is the signal intensity with no diffusion weighting and the *b-value*, defined by:

$$b = \gamma^2.G^2.\delta^2.(\Delta - \frac{\delta}{3}) \tag{2.4}$$

characterizes the parameters of the diffusion gradients in the acquisition sequence, such as duration (δ), time elapsed between the onset (Δ) and intensity of the gradients (G). Manipulating these will allow different weightings of diffusion in the acquired image. A standard value of b, for the brain, is 1000 $s.mm^{-}2$.

2.1.3.2 Single Shot Echo Planar Imaging

The Single Shot Echo Planar Imaging (SS-EPI) sequence is the most used sequence in diffusion weighted acquisition. This is due to its imperviousness to motion related artefacts and substantially low acquisition times, when compared to other sequences. During acquisition, subjects are prone to move, and this movement, during the diffusion weighting gradients application, adds a phase component to the MRI signal. This component,

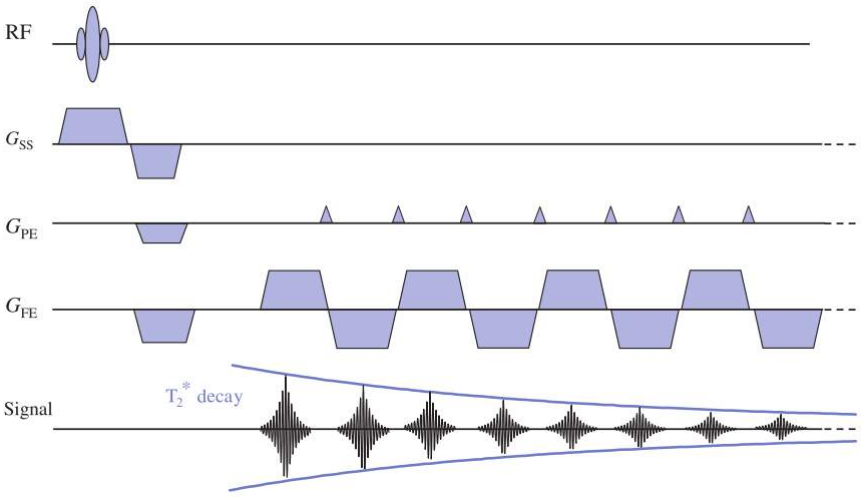

Figure 2.3: SS-EPI sequence scheme [35].

whether from head motion or from blood flow, introduces artefacts in the image that can corrupt the consistency of the acquisition if not dealt with before hand[35]. This sequence only has one RF pulse, of 180º, as seen in Fig. 2.3. Before and after the RF pulse, like PGSE, two diffusion weighting gradients are applied, but after that, a series of gradients are also applied in order to generate several gradient echos. These extra gradients are of interchangeable polarity and are responsible for the k space line coding. By manipulating these gradients' intensity it is possible to reduce the TE and obtain the desired diffusion weighting [35].

2.2 Diffusion Tensor Imaging

2.2.1 DTI Formulation and Metrics

In the previous sections, diffusion has been described only as a scalar. Although, for the sake of characterizing diffusion in three dimensions and its respective anisotropy, a tensor is needed. DTI was introduced to deal with this limitation [40]. The diffusion-weighted signal S and the non-weighted signal S_0 are related according to:

$$ln\frac{S}{S_0} = -\sum_{i=1}^{3}\sum_{j=1}^{3} b_{ij}D_{ij} \tag{2.5}$$

where b_{ij} is the *b-matrix* and D_{ij} the Diffusion Tensor (DT). The *b-matrix* effectively replaces the *b-value* in the previous formulation, and is calculated based on the diffusion gradients in the acquisition sequence [41], or *b-vectors*. The diffusion tensor comes in the following form:

$$d = \begin{bmatrix} D_{xx} & D_{xy} & D_{xz} \\ D_{yx} & D_{yy} & D_{yz} \\ D_{zx} & D_{zy} & D_{zz} \end{bmatrix} \tag{2.6}$$

In DTI, non-collinear gradient directions are applied and each gradient direction accounts for water diffusion along that direction. The estimation of the DT is increasingly precise with the increasing of the amount of gradient directions, but the acquisition time also increases with the increase of gradient directions. The minimum amount of directions required to estimate D_{ij}, is, at least, 6 different non-collinear gradient directions, along with the non-weighted acquisition.

For the purpose of this dissertation, two fitting methods were used to estimate the DT, a linear regression method and a non-linear regression method. Both methods aim at minimizing the sum of squared differences error, but the first method uses a linear regression whereas the second one uses a non-linear approach, which may provide with more favourable results [42].

To better understand the DT, it is often helpful to think about its shape, i.e. , that of an ellipsoid. In an isotropic scenario, the tensor assumes a spherical shape, for D_{xx}=D_{yy}=D_{zz}=D. On the contrary, if diffusion is anisotropic, the tensor is an elongated ellipsoid along the direction of greater diffusion, as seen in Figure 2.4. The main axis represents the MDD, the eccentricity relates to the degree of anisotropy and its symmetry and the length shows the distance travelled as a result of diffusion.

Once the diffusion tensor is calculated, it is possible to estimate rotationally invariant

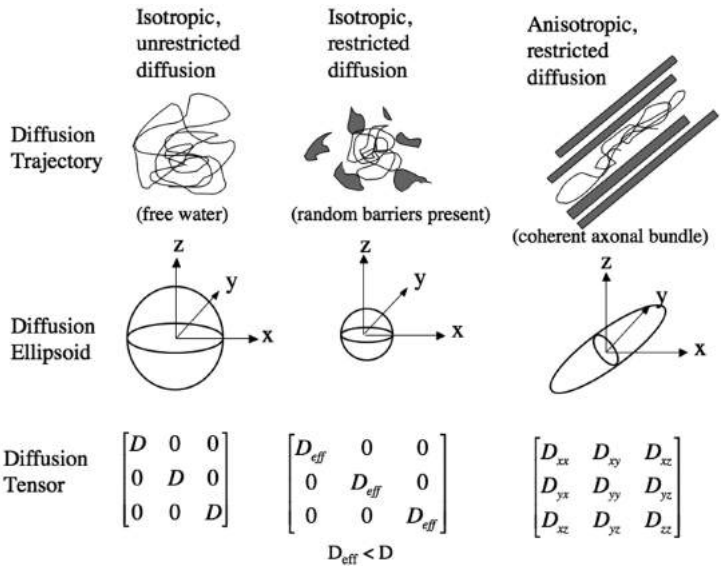

Figure 2.4: Diffusion tensor in different constriction media [43]. For unrestricted isotropic diffusion, the water molecules move freely, and the diffusion tensor has only one component in each axis. For restricted isotropic di ffusion, the lack of fixed barriers only limits the distance travelled and not its direction, which makes the diffusion tensor have only one component in each axis, although smaller than that of unrestricted diffusion. For anisotropic restricted diffusion, the molecules are restricted to a determined direction, resulting in a diffusion tensor that has three components on each axis.

parameters, i.e. independent of the reference frame, like Mean Diffusivity (MD), Fractional Anisotropy (FA), Axial Diffusivity (AD) and Radial Diffusivity (RD). This independence is derived from the fact that these indices are calculated based on the eigenvalues of the diffusion tensor. The eigenvalues provide a framework that is specific to each voxel, which means it is independent of other reference frames, like the reference frame of the scanner. The invariant measurements yield important information used to infer on the microstructures present in each voxel, and also in fibre tracking. MD represents the mean of the diffusion among all three directions, so it is determined using the following equation:

$$MD = \frac{Tr(D)}{3} = \frac{D_{xx} + D_{yy} + D_{zz}}{3} \tag{2.7}$$

where Tr(D) is the trace for the diffusion tensor. FA is a measurement of the anisotropy inherent to each voxel [44]. It can range between 0, which means the diffusion is isotropic, and 1, which means that the diffusion happens in one direction only. Consequently, tissues with microstructures which force diffusion to have anisotropic properties will be associated with FA values closer to 1, such as the white matter in the brain, while tissues such as grey matter, tend to display near isotropic di ffusion, e.g. associated with low values of FA. To calculate the FA, the eigenvalues λ for each axis of the diffusion tensor must be calculated first. By convention, the first eigenvalue λ_1 gives the AD, which reflects the magnitude of diffusion along the principal component of the diffusion ellipsoid. The eigenvalues λ_2 and λ_3 are used to calculate the RD, i.e. the diffusion along the other two components of the diffusion ellipsoid, with

$$\lambda_\perp = \frac{\lambda_2 + \lambda_3}{2} \tag{2.8}$$

The FA then comes as

$$FA = \frac{\sqrt{3[(\lambda_1 - (\overline{\lambda}))^2 + (\lambda_2 - (\overline{\lambda}))^2 + (\lambda_3 - \overline{\lambda}))^2]}}{\sqrt{2(\lambda_1^2 + \lambda_2^2 + \lambda_3^2)}} \tag{2.9}$$

where λ is the mean value of the eigenvalues

$$\overline{\lambda} = \frac{1}{3}\sum_{i=1}^{3} \lambda_i \tag{2.10}$$

2.2.2 DTI Advantages and Pitfalls

By characterizing the direction of diffusion, DTI has an unique advantage in clinical applications, when compared to other diffusion MRI techniques. Analysis of white matter pathology, like ischemia, axonal damage and myelination, tumor characterization and surgical planning are a few of its clinical applications.

However, the DTI model shows a few drawbacks. The major drawback, and the only one addressed in this dissertation, is the diffusion is modelled by a Gaussian distribution.

The fitting to the data acquired is accomplished assuming that the random displacement of the water molecules follows a Gaussian model [45]. This means that the water molecules displacement distribution function can be described by a Gaussian curve. But in the human brain context this cannot be applicable. Such fitting proves to be poor, due to the high degree of complexity of the microstructures present, which makes diffusion often behave differently from the Gaussian model[46]. Furthermore, in crossing fibres sections, the simple Gaussian model is also not applicable, as it assumes that only one fibre population exists per voxel. In these regions, the fractional anisotropy seems to be lower, due to the contribution of two or more fibres in different directions and the MDD cannot be attributed correctly. In further applications like Tractography (see 2.4), a poor characterization of MDD can result in a reconstruction of false positive or false negative tracts, which in turn introduces anatomical inaccuracies in the tractography.

2.3 Diffusion Kurtosis Imaging

As stated before, DTI is based on Gaussian model fitting, yet this fitting yields non-optimal results for biological tissues with highly complex microstructures. DKI is a method that replaces the Gaussian model by a kurtosis based model. Kurtosis is a statistical measurement that determines the deviation of a distribution in relation to a Gaussian distribution, measured by a parameter K. If $K>0$, the distribution is more concentrated around the mean value; if $K=0$ the distribution is Gaussian; if $K<0$ the tails of the distribution are wider and its peak lower, compared to those of a Gaussian. Although K can be positive or negative, in biological tissues, K has been shown to have only positive values [47].

DKI is compatible with multi-shell acquisitions, i.e. multiple b-values. This means that the acquisition times are increased when compared to those of DTI. A DTI sequence may take 3-6 mins [48] and a DKI sequence takes about 10 mins [49]. This makes DKI a feasible technique in the clinical scope, which can ease the transition from DTI to DKI from a clinical stand point, and ultimately replace DTI as the main DWI technique in the clinical context.

2.3.1 DKI Formulation and Metrics

The Kurtosis Tensor (KT), unlike DT, is a 3x3x3x3 matrix. This allows for an improved characterization of the non-Gaussian diffusion in space. To estimate such a tensor, at least 15 non-collinear diffusion gradients must be applied, beyond the 6 required for the DT, with no less than three *b-values*. Just like for the DT, two fitting methods were used to estimate the KT. The first one was Ordinary Least Square (OLS) and the second one was Constrained Least Square (CLS). The OLS method is a standard method which finds the optimal solution that minimizes the sum of squared differences error. But OLS can provide implausible estimates for the KT in biological tissues. So, to account for this

limitation of OLS, CLS uses constrains in the estimates to ensure that the tensor assumes plausible biological values.

The signal acquired by the receive coils is quantified using

$$ln\frac{S}{S_0} = -bD_{app} + \frac{1}{6}b^2D_{app}^2K_{app} \tag{2.11}$$

where D_{app} and K_{app} are the apparent diffusion and kurtosis. These relate to the diffusion and kurtosis tensors, D_{ij} and W_{ijkl} respectively, in the following way:

$$D_{app} = \sum_{i=1}^{3}\sum_{j=1}^{3} n_i n_j D_{ij} \tag{2.12}$$

$$K_{app} = \frac{MD^2}{D_{app}^2}\sum_{i=1}^{3}\sum_{j=1}^{3}\sum_{k=1}^{3}\sum_{l=1}^{3} n_i n_j n_k n_l W_{ijkl} \tag{2.13}$$

were n is the unit vector that describes the direction of the diffusion gradient.

Analogously to DT, KT also has some important rotationally invariant measurements associated to them: Mean Kurtosis (MK), Axial Kurtosis (AK), Radial Kurtosis (RK) and Kurtosis Fractional Anisotropy (FA_K)[47]. MK, as MD, provides a measure of the overall kurtosis, estimated as the average of directional kurtosis, defined by:

$$MK = \frac{1}{N}\sum_{i=1}^{3}(K_{app})_i \tag{2.14}$$

To calculate the FA_K, first it is necessary to rotate the kurtosis tensor W from the Cartesian coordinate system to the coordinate system defined by the eigenvectors of D ([50])

$$\widehat{W}_{ijkl} = \sum_{i=1}^{3}\sum_{j=1}^{3}\sum_{k=1}^{3}\sum_{l=1}^{3} e_{i'i}e_{j'i}e_{k'i}e_{l'i}W_{i'j'k'l'} \tag{2.15}$$

where e_{ij} are the elements of the 3D rotation matrix defined by the eigenvectors and $\widehat{W}_{ijkl}$ the elements of the rotated kurtosis tensor. Once $\widehat{W}_{ijkl}$ is computed, the values of the kurtosis tensor on the diffusion ellipsoid three main axes, with i=1, 2 and 3, are determined by

$$\kappa_i = \frac{MD^2}{\lambda_i^2}.\widehat{W}_{iiii} \tag{2.16}$$

resulting in AK being

$$\kappa_{\|} = \kappa_1 \tag{2.17}$$

and RK

$$\kappa_{\perp} = \frac{\kappa_2 + \kappa_3}{2} \tag{2.18}$$

similarly to the DTI analogous measurements. Finally, FA_K comes as

$$FA_k = \frac{\sqrt{3[(\kappa_1 - (\overline{\kappa}))^2 + (\kappa_2 - (\overline{\kappa}))^2 + (\kappa_3 - (\overline{\kappa}))^2]}}{\sqrt{2(\kappa_1^2 + \kappa_2^2 + \kappa_3^2)}} \tag{2.19}$$

where κ is the mean value of the kurtosis over the diffusion ellipsoid

$$\overline{\kappa} = \frac{1}{3}\sum_{i=1}^{3}\kappa_i \tag{2.20}$$

FA_K is close to one when there is a value of κ_i substantially larger than the other two, and close to zero when all three values of κ are similar to each other.

2.3.2 DKI Advantages and Pitfalls

The DKI model has similar applications in the clinical scope to those of DTI. Additionally, it can provide with more detailed information about tissue microstructure, and even perform biological modelling of diffusion [51]. As opposed to DTI, DKI can account for multiple fibre populations in the same voxel, which may result in more anatomically accurate tractography.

This model also has its own pitfalls. For being a fairly recent technique it is still not very established. For that reason, it isn't often used in the clinical scope, it is still considered only as a research tool. Furthermore, the longer acquisition times and more stringent hardware requirements, due to high gradient strength for example, can be a deterrent from using this technique.

2.4 Tractography

One of the primary applications of the information on the direction of diffusion is fibre tract reconstruction, or tractography. The main purpose of tractography is to determine intervoxel connectivity based on the anisotropic diffusion of water [6]. In this section we will cover the tractography algorithms performed, for both DTI and DKI-based tractographies.

2.4.1 DTI-based Tractography

DTI Fibre tracking is based on the assumption that a tract can be represented as a curve in space[7], using the Frenet equation:

$$\frac{dr(s)}{ds} = t(s) \tag{2.21}$$

were r(s) is a vector, parameterized by the arc-length, s, of the trajectory, and t(s) is the unit tangent vector to r(s) at location s.

Since there is no way of calculating the tangent vector through analytical processes, numerical methods, like Euler integration and Runger-Kutta methods, were first used [7]. DTI-based tractography algorithms have since evolved and can now be divided into 3 classes:

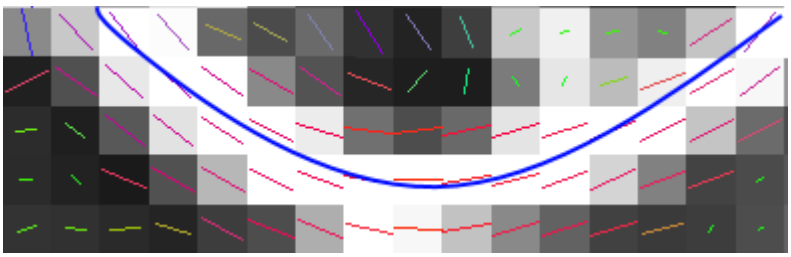

Figure 2.5: Fibre reconstruction from the main diffusion direction map. The blue line indicates the path that a tract follows during reconstruction, and the lines represent the main diffusivity direction for each voxel.

1. **Deterministic**, characterized by the assumption that the principal eigenvector is parallel to the dominant direction of the fibre, with integration of neighbouring pixels to define smooth trajectories [40]. The tangent vector is then determined by the eigenvector ϵ_1 associated with the largest eigenvalue, λ_1 of the diffusion tensor, using the following relationship:

$$t(s) = \epsilon_1(r(s)) \tag{2.22}$$

Combining the equations 2.21 and 2.22, we obtain

$$\frac{dr(s)}{ds} = \epsilon_1(r(s)) \tag{2.23}$$

which can be solved forcing the initial condition for each tract to be

$$r(0) = r_0 \tag{2.24}$$

where r_0 is the starting point for a given tract. This translates into an iterative method of fibre tracking, starting in one point and recursively following the di ffusion "path" through the main diffusivity direction for each voxel, given by the DT greater eigenvalue. Figure 2.5 shows the the reconstruction based on the principal eigenvector.

2. **Probabilistic**, in which the most favourable path between predetermined regions is evaluated. To do this, probabilistic maps of fibre connectivity for the whole brain are computed. This approach is different from the deterministic because the tracking is computed along a continuous line, instead of a discrete vector [9];

3. **Global**, which estimates the local fibre orientations and then propagates them throughout the voxels to obtain estimates of connections between several brain locations, using a Bayesian propagation model [52].

However, they all share common grounds as to how to generate a tract [53]:

- reconstruction is terminated if the streamline enters a region where the FA is below a predetermined threshold. This condition is imposed so that the fibre reconstruction does not occur in regions where diffusion is not anisotropic, such as grey matter;

- reconstruction is terminated if the maximum angle that is taken between voxels is above a predetermined threshold. This condition avoids the reconstruction of spurious tracts as a result of sudden changes in direction from one voxel to another.

Only deterministic algorithms were performed throughout this study, but the other algorithm categories were presented to give the reader the full scope.

DTI-based tractography, as seen before, has a significant pitfall, which is the fact that it cannot reliably predict fibre population directions for voxels with two or more intersecting populations. So there is a need to introduce models that can deal with this problem, often called "fibre crossing problem" [15, 55, 56].

2.4.2 DKI-based Tractography

DKI-based tractography is yet to be fully optimized, with only two methods created thus far. Both methods were incorporated in this dissertation and later on compared for performance.

2.4.2.1 Orientation Distribution Function based Tractrography

The first method to reconstruct fibres from DKI was based on the diffusion Orientation Distribution Function (dODF), proposed by Lazar et al. in 2008 [54], and later on optimized [57]. dODF is a function that characterizes the spacial orientation of a distribution, in this case water diffusion, and is defined by:

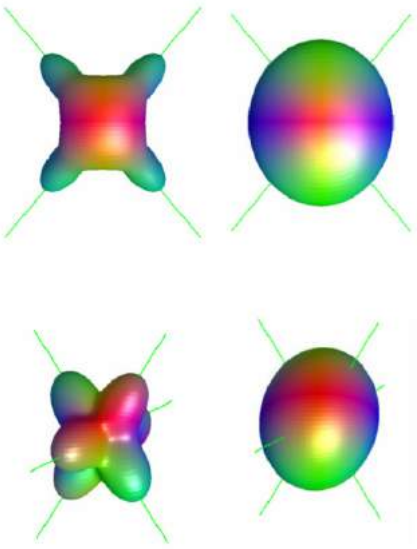

Figure 2.6: 3D geometry of DKI-ODF (left) and DTI-ODF (right). The DKI-ODF is able to account for the fibre crossings, for two fibres (top left) and three (bottom left), whereas DTI-ODF shows a geometry similar to that of isotropic diffusion. Adapted from [54].

$$\Psi_\alpha(\hat{n}) = \frac{1}{Z}\int_0^\infty s^\alpha ds P(s\widehat{n}, t) \tag{2.25}$$

where $\Psi_\alpha(\hat{n})$ is the dODF in a direction given by a unit vetor $\hat{n}$, $P(s,t)$ is the water diffusion displacement Probability Density Function (dPDF) for a molecular displacement s over time t. If the dPDF is approximated by a Gaussian model, the results are the same as those obtained by the DTI, and therefore, the shortcomings are also the same. Therefore, the dPDF is aproximated using non-Gaussian models, in particular the kurtosis model, extracted from the kurtosis tensor (DKI-ODF) [54]. From that, it is possible to obtain the directions of multiple fibre bundles in each voxel, as shown in figure 2.6, up to three directions.

2.4.2.2 Maxima Kurtosis based Tractography

The KT, for being a forth order tensor, yields a better spacial characterization of the spacial arrangement of tissue microstructure. In a preliminary DKI study, KT geometry showed maxima perpendicular to the direction of well-aligned fibres [49], therefore, there is a correlation between the geometry of the tensor and the spacial arrangement of the fibres. This was then used by Neto Henriques et. al [51], for proposing an algorithm to reconstruct fibre tracts based on the KT maxima perpendicular directions(see Figure 2.7). By estimating the KT's maxima, it is possible to detect multiple fibre populations within a voxel, up to three, like the DKI-ODF method.

This method deals not only with the limitations of DTI, but also has been shown to have smaller angular errors for fibre crossing than DKI-ODF [51], which may result in better fibre tracking. However, it also has its own pitfalls. DKI-KT was shown to be more sensitive to multi-compartmental model parameters than DKI-ODF. When applied to

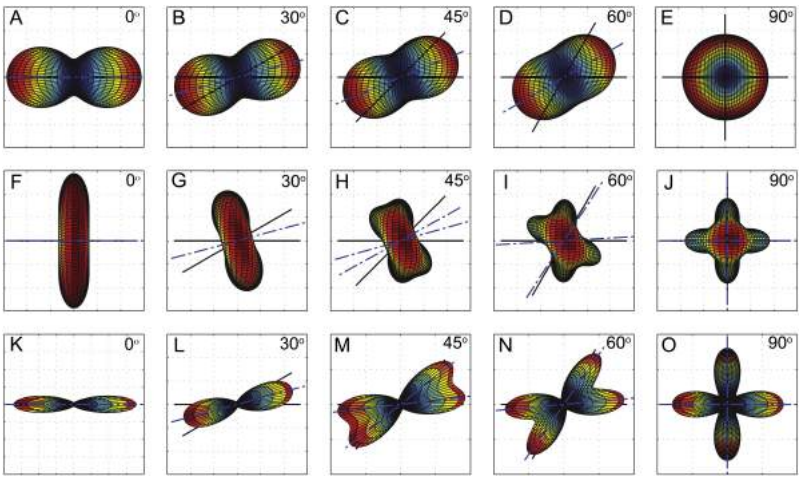

Figure 2.7: 3D geometry of DT (Panels A-E), KT (Panels F-J) and ODF (Panels K-O), for crossing fibres of 0º, 30º, 45º, 60º and 90º [51]. The DT is unable to deal with crossing fibres, whereas KT shows maxima perpendicular to the directions of the fibres and ODF shows maxima in the direction of the fibres.

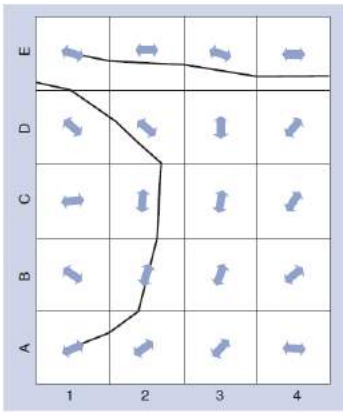

Figure 2.8: Noncommutative properties of tractography algorithms [53].

real brain data, this could lead to a less stable performance of fibre tracking across the different regions [51].

2.4.3 Tractography Overall Shortcomings

Despite providing a unique perspective of white matter tracts, tractography reconstruction also has its own shortcomings. Due to the symmetry of the diffusion phenomena, there is no way of distinguishing between afferent and efferent connections. Adding to that, tractography is not commutative. This means that, starting from one point we end up going to another, but the reconstructed tracts might be different if the reconstruction was to be done in reverse, as seen in figure 2.8.

2.5 Brain Connectivity

The brain is regarded as a highly complex network, comprised of numerous interconnected processing regions. Gathering the information provided by the tractography reconstruction, it is possible to characterize the brain's complex system through a small number of neurobiologically relevant and easily computable measures, by means of complex network analysis[58]. Complex network analysis comes from a mathematics branch called graph theory, used in the study of graphs. These structures are used to model pairwise relations between objects. Unlike graph theory, which often deals with small and "well-behaved" networks, complex network analysis deals with real-life networks both large and complex [58].

Brain networks fall into three categories:

Structural The brain regions are considered connected when there are physical connections between them, i.e. white matter tracts.

Functional Establishes a correlation between time and activity between brain regions, regardless of anatomical connection.

Effective Relates two brain regions regarding their intrinsic causality, i.e. how the behaviour of the first region influences the second one.

In this work, only the structural connectivity of the brain will be addressed.

2.5.1 Networks: Principles and Definitions

A network is defined by a set of nodes which are connected to each other via edges, and can be represented via graphs (Figure 2.11). The properties of the networks are determined by their links. Depending on the links characteristics, the network can be classified in four different ways:

Binary undirected network This type of network is defined by having bidirectional links, and all have the same weight. What this means is that all links have the same importance to a node they connect to, and that the link can either go from node A to node B, or the other way around;

Weighted undirected network Differs from the previous one by associating a weight to each link. A link with a higher weight will be privileged over another with a lower weight. The links are still bidirectional;

Binary directed network This network is similar to the first one but the links are unidirectional, representing the flow from A to B, but not necessarily the other way around.

Weighted directed network The latter type of network is defined by having weighted and unidirectional links.

Relationships between these networks are better seen in Fig. 2.11.

To better understand these networks, connectivity matrices are computed, which correlate each node's connectivity to all the other nodes in the network. These matrices are the input for the complex network analysis.

2.5.2 Complex Network Analysis Metrics

Complex network analysis metrics hold the advantage of quantifying the parameters that allow for a complete examination of the networks topology and efficiency. This examination can happen from two standpoints: a segregation standpoint, which yields information about the clusters of nodes, inferring on characteristics regarding these clusters, as opposed to a single node; and the integration standpoint, determining the characteristics inherent to each node and how they relate to the surrounding nodes. Among the many metrics, the ones deemed most important are described below. For further reading, see [58].

Degree of a node The number of links that are associated to that node. This is a core measurement, as many other measurements are intertwined with this one;

Strength Sum of all of the link's weights;

Clustering coefficient Defined locally as the fraction of triangles around an individual node. It is equivalent to the fraction of that node's neighbours that are also each other's neighbours;

Modularity Statistical measurement that determines the number of non-overlapping modules (Community Modules);

Motif Small sub-network of nodes and links. Motifs are regarded as the network's "building blocks" [59];

Characteristic path length (λ) Shortest path from node A to node B;

Radius Minimum distance between two nodes;

Diameter Maximum distance between two nodes;

Global efficiency Inverse of the characteristic path length;

Eccentricity Length of the maximum short path between two nodes;

Betweenness centrality Fraction of the paths that contain a specific node;

Edge betweenness Fraction of the paths that contain a specific link;

Hub Node that has a high degree, acting as a central piece of the network.

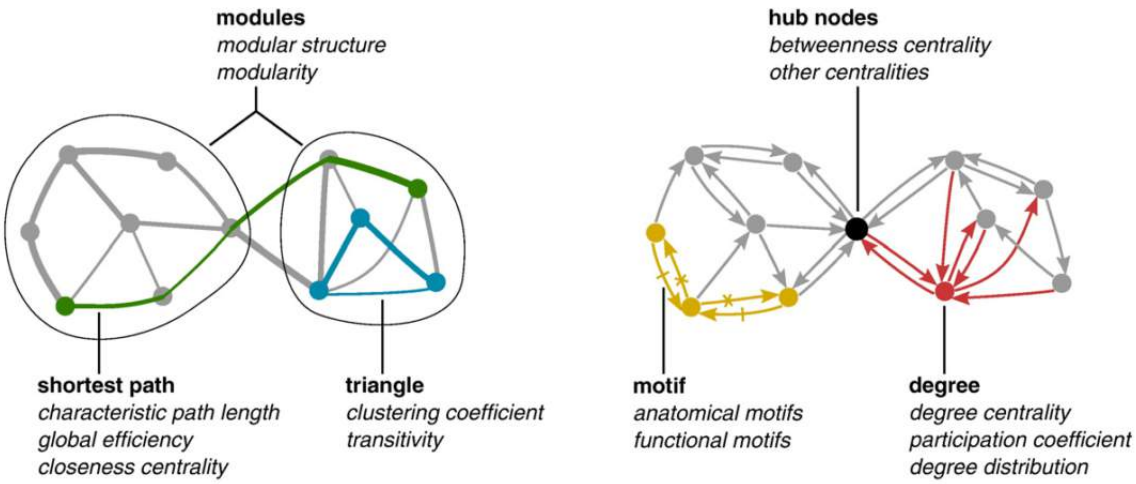

Figure 2.9: Graph metrics[58]. These metrics are based on basic connectivity properties (gray). Integration metrics involve shortest path (green) while segregation are often based on the clustering coefficient (blue). Centrality metrics should involve degree (red). Hubs (black) have a high degree since they partake in a high number of paths, consequently having higher betweenness centrality. Local patterns are quantified by motifs (yellow).

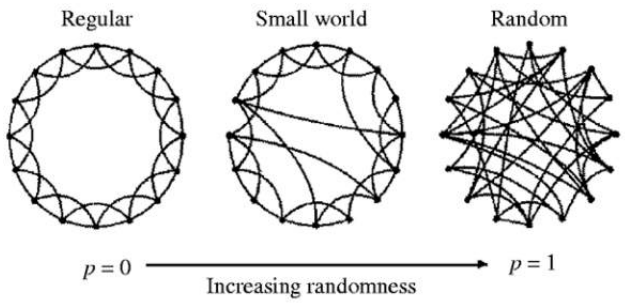

Figure 2.10: Three types of network configuration[60]. The parameter p is the degree of randomness. Ranging from 0 to 1, it expresses how random the network is, being 0 the lack of long range connections while having dense small clusters, and 1 the lack of local small clusters while having long range random connections.

Participation Coefficient Measure of diversity of intermodular connections of individual nodes.

A network can be characterized by its λ, global efficiency, eccentricity, radius and diameter [60]. A depiction of these metrics can be found in Figure 2.9.

2.5.3 Brain Network

As seen before, the brain can be viewed as a group of neurons sharing information between them and between nervous centres. This way, it is acceptable to consider the brain as a very complex network, and thus viable to study its connectivity through the methods discussed above. Studies have shown that the brain is in fact made of clusters grouped in cortical regions which are connected [58, 61].

A network can have an intrinsic configuration, which can be categorized using its degree of randomness (Fig. 2.10). This randomness can range from 0 to 1, with 0 being completely regular and 1 completely random. Brain network configuration has been found to have an intermediate configuration, similar to that of a *small-world* network, in which there are dense short distance clusters and some long distance connections. *Small-world* networks have, consequently, high clustering coefficients, short characteristic paths and repeating motifs along the network. This small-worldness (ω) can be measured by comparing the network's path length, λ, and clustering coefficient, C, and comparing those to the path length of an equivalent random network λ_{rand} and the clustering coefficient of an equivalent lattice network, C_{latt}, using the equation:

$$\omega = \frac{\lambda_{rand}}{\lambda} - \frac{C}{C_{latt}} \tag{2.26}$$

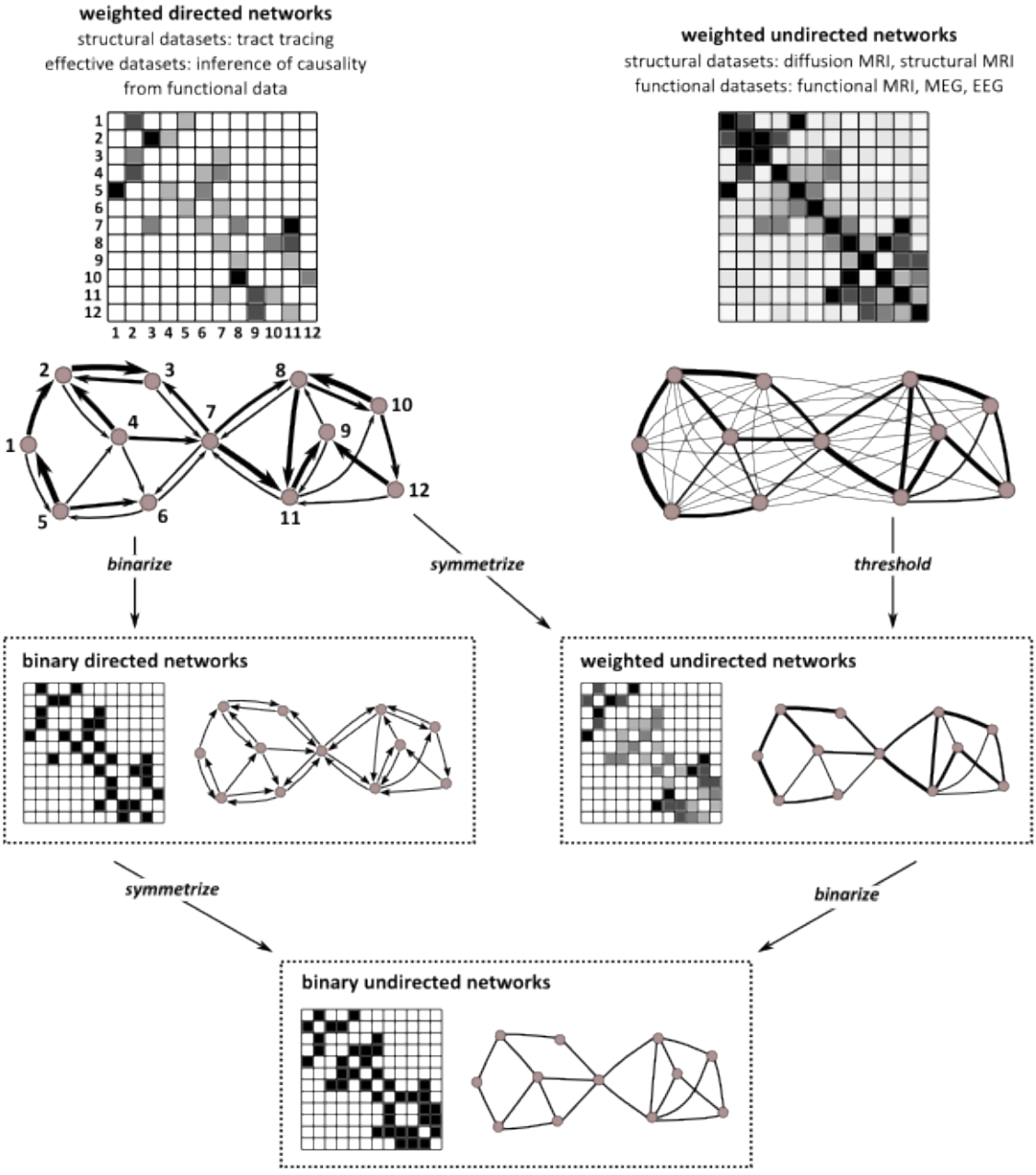

Figure 2.11: Diagram showing the relationships between all types of networks [58].

Chapter 3

Materials and Methods

The main focus of this dissertation is to evaluate the performance of the DKI-based tractography over DTI-based tractography, and how it affects brain connectivity estimates. This difference is expected to be blatant in crossing fibre regions, where, as stated in the previous chapter, DKI can account for multiple fibre populations intra-voxel, whereas DTI cannot.

In this chapter, the reader is presented with the materials and methods used throughout this study in order to accomplish the dissertation's objective. Firstly, there will be a brief description of the dataset used, the equipment and acquisition schemes. Afterwards, the image processing methodology will be described, step-by-step. Finally, the methods of statistical treatment of the data will be presented.

3.1 Dataset and Acquisitions

The dataset used in this study is made up of acquisitions in six healthy subjects, three females, with mean age ± standard deviation of 30 ± 5 years.

Two MRI data types were acquired for each subject: T1-weighted anatomical MRI (aMRI) and DWI. Both modalities were acquired using a 3 Tesla Siemens Trio scanner with a 32-channel head coil, from the MRC Cognition and Brain Unit, in Cambridge, UK, as part of a data partnership established between the MRC-CBU and IBEB.

The acquisition specifications for the T1-weighted MRI were as follows: Magnetization Prepared Rapid Gradient Echo (MPRAGE) sequence, with Repetition Time (TR)=2250 ms, Echo Time (TE)=2.98 ms, Inversion Time (TI)=900 ms, Field of View (FOV)=$256x256mm^2$, voxel size 1x1x1 mm^3 and 192 slices.

The DWI acquisition specifications were: Twice Refocused Spin Echo (TRSE) echo-plannar imaging sequence, with TR=9400 ms, TE=104 ms, acquisition matrix = 94x94,

voxel size of 2x2x2 mm^3, non-zero b-values of 1000 $s.mm^{-2}$ and 2000 $s.mm^{-2}$, each b-value with 64 equally spaced gradient directions. Also 6 b-value = 0 $s.mm^{-2}$ were acquired, with 3 in the beginning of the acquisition and the remaining 3 in between the non-zero b-values acquisition. The whole DWI acquisition composed the DKI dataset, whereas the DTI dataset was extracted from the whole set using the first 3 b-0 images and images with non-zero b-value of 1000 $s.mm^{-2}$.

3.2 Image Processing Tools and Steps

The main tools used to process the dataset were in-house built Matlab toolboxes entitled Multimodal Imaging Brain Complexity Analysis (MIBCA) [62] and United Dffusion Kurtosis Imaging (uDKI) [63].

MIBCA was used for its ability to process multi-modal imaging and connectivity data while also bringing the advantage of working in pre-established standardized processing pipelines, reducing the time wasted between steps. This toolbox uses third party software, such as *Freesurfer*, *FMRIB Software Library (FSL)*, and *Statistical Parametric Mapping (SPM)*, to perform the data processing. These software compile the most robust methods of image processing used in the literature.

uDKI was used for being the only tool currently available that can estimate the kurtosis tensor's related metrics and also reconstruct the fibre tracts based on the said tensor [51].

For faster use and better convenience, both toolboxes were later on merged so that MIBCA would also be able to work with DKI data, using the uDKI functions.

The dataset, due to its multi-modality nature, underwent two different processing pipelines. Nevertheless, all the images were first converted from DICOM to NIFTI, using MRIcron's function *dcm2nii*.

The aMRI processing steps were accomplished using the MIBCA aMRI pipeline, using the Freesurfer function *recon-all*. The general traits of the function are:

- Spatial alignment of the subject's brain according to a standard space (MN1_152_1mm). This will generate transformation matrices, which will then be used to transpose each Region of Interest (ROI) into the DWI space;
- Brain segmentation and parcellation using the Desikan-Killiany brain atlas [64]. This segmentation provided a list of ROI to be analysed in future steps.

As for the DWI processing steps, both DTI and DKI were first corrected for eddy current distortions, using FSL's function *eddy_correct* [65], and then a brain mask was created using FSL's *Brain Extraction Tool (BET)* [65]. Afterwards, the DTI dataset was processed, using uDKI, as follows:

- Diffusion tensor estimation. The diffusion tensor was estimated using a linear model and also a non-linear model, described in 2.2.1. In this same step a computation of

a b0 image (non-weighted) was performed, from the mean of all of the b0 images acquired. This image will be used to register the ROI's in the DWI space;

- Diffusion tensor related metrics estimation, like FA, AD, RD, MD and MDD;
- DTI-based tractography reconstruction, based on the MDD and FA maps. The algorithm used for this reconstruction was a streamline brute force first order Euler algorithm [66].

The DKI dataset underwent similar steps.

- Gaussian filter (FWHM=1.5 pixels) to smooth images and increases signal-to-noise ratio of the image. Since DKI is much more sensitive to noise than DTI, this is a critical step for DKI.
- Kurtosis tensor estimation. The kurtosis tensor was estimated using the OLS and the CLS algorithms, described in 2.3.1. The computation of a b0 image (non-weighted) was performed, similarly to the DTI processing pipeline, also used in ROI registration;
- Diffusion and kurtosis tensor related metrics estimation, like FA, AD, RD, MD and MDD for diffusion tensor, and AK, RK, and MK for the kurtosis tensor;
- Kurtosis tractography related map estimation, such as fibre directions and number of fibres per voxel maps. These maps were used in the tractography step.
- DKI-based tractography reconstruction. This reconstruction was made using two different algorithms: the first was DKI-ODF [57] and the second one was performed using DKI-KT [51].

In order to visually inspect and validate the tractography results, *TrackVis* was used, a 3D tractography visualization software. With it, we were able to isolate tracts emerging from and to predetermined ROI. These ROI were related to Cortico-Spinal Tracts (CST) and Corpus Callosum (CC). The reason being that the CST tracts cross the CC tracts, and thus there are voxels in which there are more than one fibre population. TrackVis offers the option of displaying the tracts intersected by any number of ROI, thus isolating tracts of interest. Both CST and CC tracts were isolated using hand-drawn ROI, based on [67]. For the CST tracts isolation, ROI's were placed in the Internal Capsule (IC), of both hemispheres, and in the cortical regions of Superior Frontal, Paracentral Lobule and Pre-Cuneus. For the CC tracts isolation, a single ROI was used, extending through the length of the body of the Corpus Callosum. The placement of the ROI is shown in Figure 3.1.

Once the tracts were computed and validated, the connectivity processing took place. To begin, the labeled ROI and their respective transformation matrices, generated from T1 images, were gathered to perform segmentation of the DWI images. This is accomplished

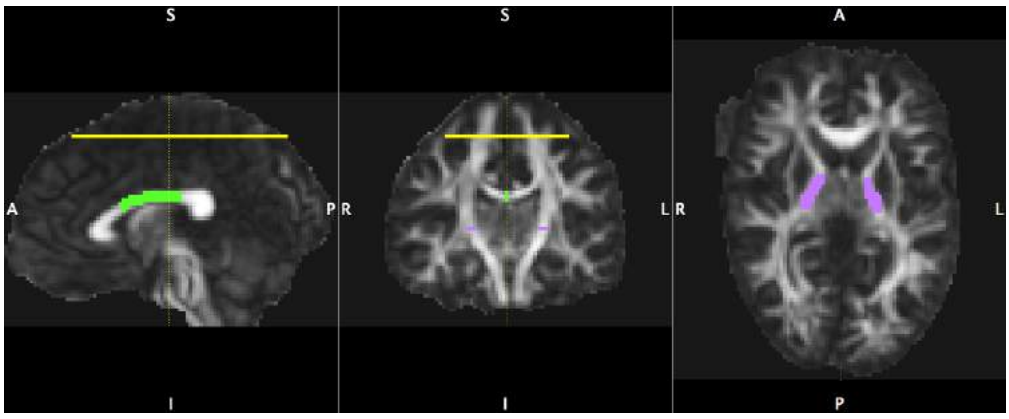

Figure 3.1: Generic placement of the ROI's for tract isolation based on [67]. The IC ROI (purple) and the cortical regions ROI (yellow) served to isolate the CST, and the CC is isolated by considering the tracts that go through the green ROI.

by, based on the subject's b0 image, considering the affine transformations between a DWI volume to T1. Then, non-linear transformations perform the final alignment of the ROI and finally the B0 image is parcellated accordingly. This step is performed automatically by MIBCA, resorting to FSL's *flirt* and *fnirt* functions.

After the parcellation of the brain is completed, an adjacency matrix can be calculated, gathering the information on the number of streamlines connecting each pair of ROI. And finally, from the adjacency matrix it is possible to extract the connectivity metrics for each subject, using the *Brain Connectivity Toolbox (BCT)* [58].

The global connectivity metrics computed were: Transitivity, Characteristic Path Length, Global Efficiency, Modularity and Small Worldness. The local connectivity metrics computed were: Betweenness Centrality, Clustering Coefficient, Node Degree, Eccentricity, Local Efficiency, Community Modules and Participation Coefficient.

Apart from the connectivity metrics, MIBCA also extracts the values of the diffusion metrics for every ROI.

Figure 3.2 summarizes the processing steps taken and their respective outputs.

3.3 Statistical Analysis

As a final result of the processing stage, 4 different tensors were computed: Linearly fitted Diffusion Tensor (L-DT), Non-Linearly fitted Diffusion Tensor (nL-DT), Ordinary Least Squares fitted Kurtosis Tensor (OLS-KT) and Constrained Least Squares fitted Kurtosis Tensor (CLS-KT), and their respective diffusion metrics; and 6 whole-brain tractography datasets: 1 per DTI tensor (L-DTI and nL-DTI), plus 2 per each DKI tensor (OLS-DKI and CLS-DKI), corresponding to DKI-ODF and DKI-KT tract reconstructions, as well as their respective connectivity metrics.

The data to be treated are of two kinds: 1) maps of metric values per brain region, both for diffusion and connectivity metrics; 2) global connectivity metrics intrinsic to

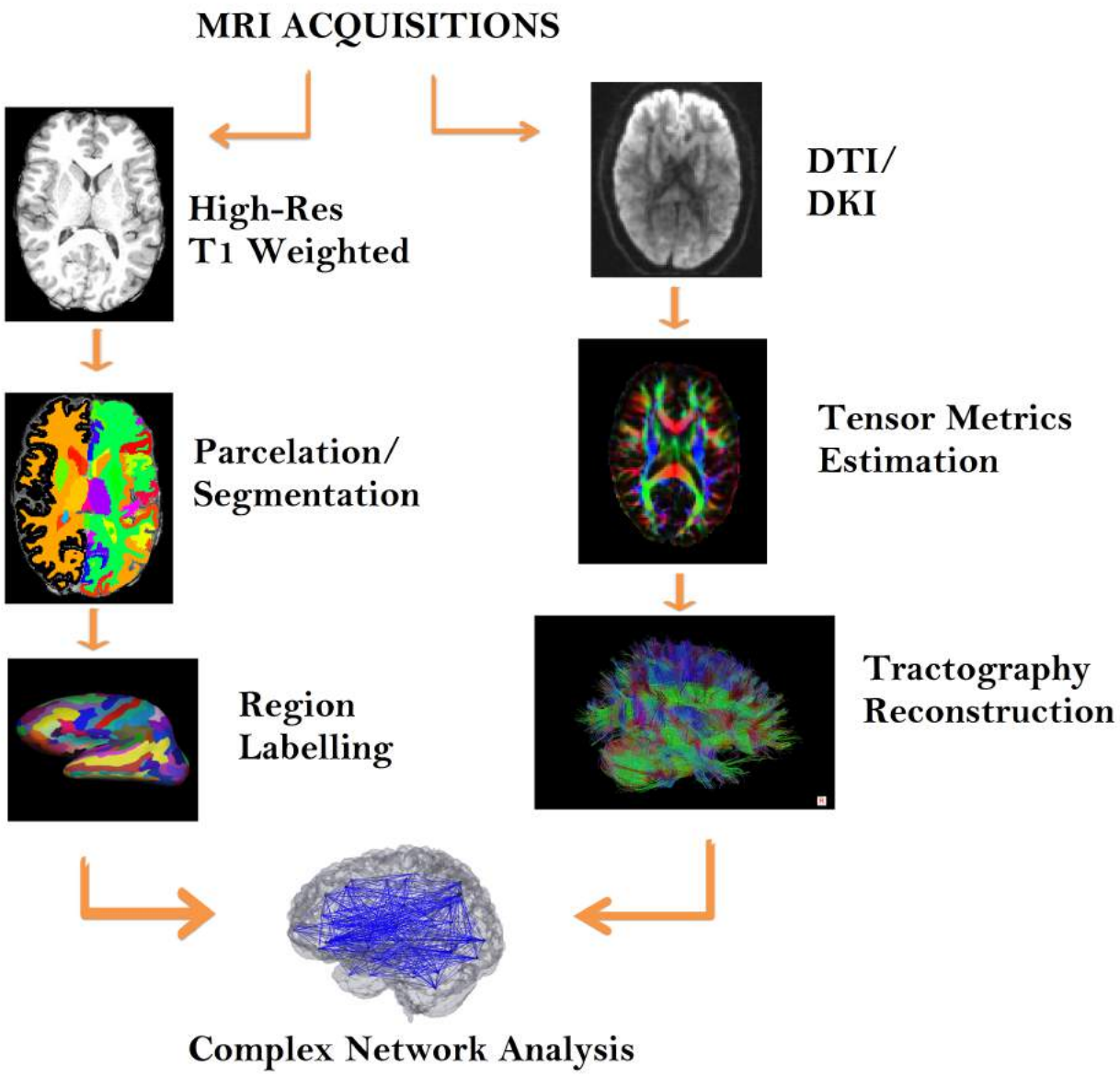

Figure 3.2: Diagram of the processing steps followed in this work.

each tractography. Global connectivity metrics are unique for each tractography, whereas local connectivity metrics and diffusion metrics were computed for each ROI in the brain. The ROI encompass 76 brain regions, 8 sub-cortical and 30 cortical, for each hemisphere (refer to A).

The global connectivity metrics were compared using the Wilcoxon's signed rank test on the mean values for all subjects, to compare between DTI and DKI based tractography sets. This statistical test checks for the null hypothesis that the difference of the pair (e.g. difference between the mean characteristic path length calculated from L-DTI and OLS-DKI based tractographies) comes from a distribution with zero median, i.e. if both

samples are statistically equal, at a 5% significance level. From that, we can tell if DKI provides with statistically different information from that provided by DTI. Later on, through the analysis of this information, we tried to determine if DKI has a better characterization of the network than that of DTI, taking into account the information from 2.5.3.

The local connectivity statistical analysis followed a different, more complex path. The general chain of thought was that the different tensors would have let to significantly different values of diffusion metrics (AD, RD, and MD) in some ROI, due to their sensitivity (or not) to multiple fibre populations. This would "flag" critical ROI, presumably with multiple voxels with multi-fibre populations, such that it would alter the di ffusion metrics values and, consequently, the connectivity metrics for that particular ROI. ROI with no significant differences in diffusion metrics are considered to be those with no relevant changes in their respective tractography, and thus, with no relevant changes in connectivity.

First of all, a normality test was needed, to check whether or not all of the diffusion parameters came from a Gaussian distribution, and so the statistical treatment of the data would be parametric. The normality test chosen was a One-sample Kolmogorov-Smirnov test, which tests the null hypothesis that the data comes from a standard normal distribution, against the alternative that it does not, at a 5% significance level. The test results rejected the null hypothesis for every diffusion metric considered, which meant that the data did not come from a normal distribution. Hence, the statistical analysis approach used was a non-parametric approach, in which no assumptions are made *a priori* regarding the data's distribution.

The next step in the local analysis was to make sure that the diffusion metrics estimated by each tensor (and each fit) were, in fact, di fferent from each other. To do this, a two-sided Signed-Rank Wilcoxon test was performed on the following pairs of fittings: L-DTI vs OLS-DKI, L-DTI vs CLS-DKI, nL-DTI vs OLS-DKI and nL-DTI vs CLS-DKI, for each of the 3 diffusion metrics, AD, RD and MD. The comparisons were aimed at assessing the differences between DTI and DKI tensor fits, to better meet the objectives of this dissertation, and tests like L-DTI vs nL-DTI were ruled out. The results of the Signed-Rank Wilcoxon test, across the board, showed that the diffusion metrics were statistically distinct for each type of fitting.

To determine the ROI that displayed significantly different diffusion metrics, the pairs of the Wilcoxon test were subtracted for all 3 diffusion metrics, so that the difference was of the type *DKI-DTI*. What this means is that for each diffusion metric, L-DTI was subtracted to OLS-DKI, L-DTI was subtracted to CLS-DKI, and so forth, for all of the 4 comparisons. This created 12 difference arrays of data, for each subject. To better understand this data, they were plotted in Bland-Altman plots [68]. The criteria used to select significantly different ROI based on the diffusion metrics was a deviation from the mean difference above twice the standard deviation of the distribution (*mean+2std*).

After the ROI had been identified for each subject, consistently "flagged" ROI were

determined. A consistently "flagged" ROI is a ROI that has been "flagged" for the majority of the subjects. This step would remove the ROI that were identified in the previous step by mere subject variability.

Then, these final lists of ROI were inspected with regards to their corresponding local connectivity data. The cohort of local connectivity metrics were compared three-by-three because, due to fact that the ROI were identified out of a pair of diffusion metric comparison, each pair of diffusion metric comparison has 3 possible tractography reconstructions (1 for DTI and 2 for DKI), and, therefore, 3 distinct connectivity metrics. The comparison of these metrics was then used to relate changes in the local connectivity metrics and the micro-structure (higher or lower degree of complexity of the structures at hand) for each ROI.

Chapter 4

Results and Discussion

In this chapter, the results will be presented, according to each study of this dissertation, first tractography related results, then connectivity related results.

4.1 Tractography

Figure 4.1 is the coronal view of the isolated tracts defined in 3.2, for a representative subject for all 6 tractography reconstructions. In red are represented the CC tracts, and in cyan the CST. For the full array of tractography datasets, please refer to Appendix B.

In panels A and B, the L-DT and nL-DT reconstructions, respectively, show the CC tracts "encapsulated" by the CST, with no evidence of crossing fibres between both structures. Panels B and C show the results for the DKI based tractography methods, algorithms KT and ODF respectively, when the tensor is estimated using OLS method. In these it is possible to distinguish a few sections in which there are crossing fibres, particularly, in the region of the body of the CC. Finally, Panels D and E show the tractography results for DKI-KT and DKI-ODF reconstructions, respectively, in which the tensor was estimated via CLS method. This method shows the most amount of tracts crossing between the two structures at hand.

Number of tracts, number of occupied voxels and volume statistics were also obtained for all subjects and tractographies. These results are shown in Table **??**. DKI-ODF methods seem to show increased numbers across the board, with the CLS-ODF method being the highest. DKI-KT methods show the lowest numbers, but only for the CST tracts. This limitation may be due to fact that, these ascending CST tracts, towards the pre-central gyrus, follow a more concave and convex pathway. This, in turn, reflects on small fanning angles, which are better resolved using the DKI-ODF method [51]. DTI methods yield better tract numbers for the CST, when compared to DKI-KT. Although, they fail to

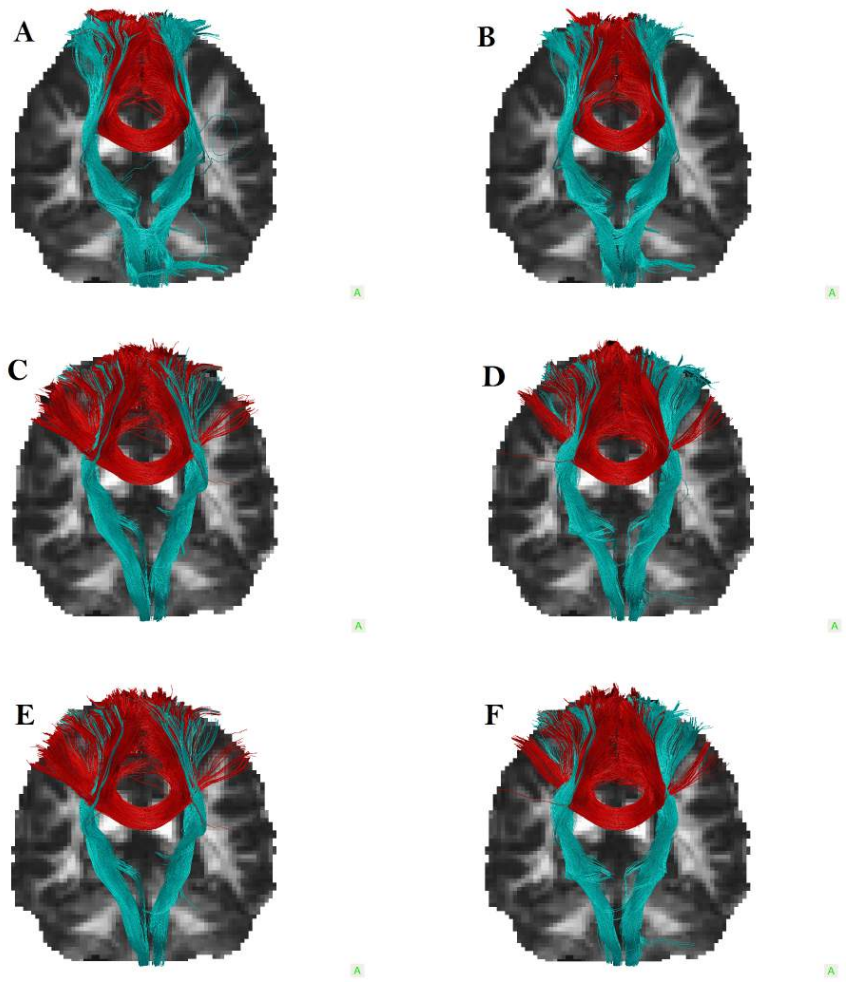

Figure 4.1: Tractography reconstructions for Subject 1. In cyan the CST tracts, red the CC tracts. In panels A and B, the L-DT and nL-DT reconstructions, respectively, panels B and C show the results for the OLS-KT and OLS-ODF, and panels D and E show the tractography results for CLS-KT and CLS-ODF reconstruction.

improve over any of the DKI based tractographies in the CC structure. Such difference is caused by the inability to resolve the crossing fibres between CC and CST, which drastically reduces the number of isolated tracts, and consequently the number of occupied voxels and volume.

Furthermore, an additional inspection was performed to understand to what extent the eigenvectors information was misinterpreted in the crossing fibre regions. To do so, misinterpreted tracts were identified and isolated to better illustrate this pitfall's consequences, shown in Figure 4.3. This misinterpretation has two causes: misaligned MDD (Figure 4.3-A) or corrupted FA (Figure 4.3-B). In the first case, the reconstruction leads to an erroneous reconstruction, where CST tracts become CC tracts in the crossing fibres region. The latter displays voxels in which FA was deemed lower than the threshold defined for the reconstruction algorithm. This is due to the contribution of all of the crossing populations, each contributing in their own direction. Since FA reaches values

below the defined threshold, the reconstruction is terminated, leaving unfinished tracts.

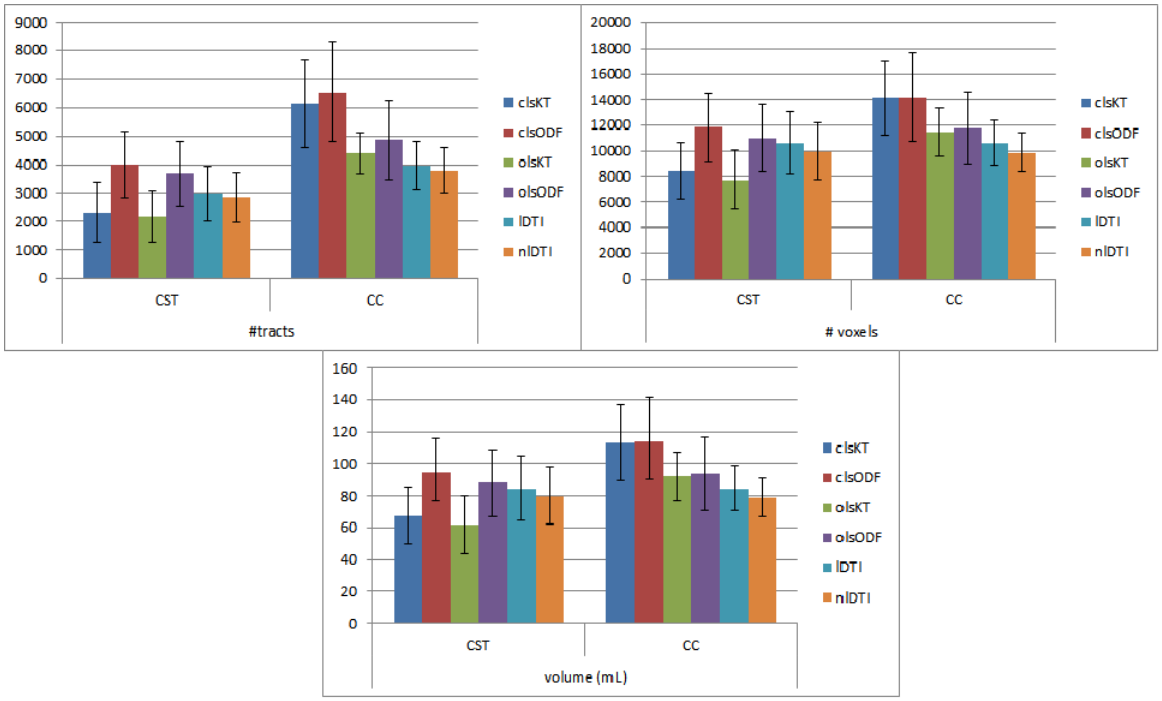

Figure 4.2: Bar plots of the streamline statistics for the mean values of all 6 subjects. The top right plot is the number of tracts per tractography computation, in each region. On the top right it's the number of occupied voxels by the computed tracts in each structure, for all of the tractography methods. On the bottom, the volume occupied by the computed tracts in each structure, for all of the tractography methods. The vertical lines represent the standard deviation of the computed tracts for all 6 subjects.

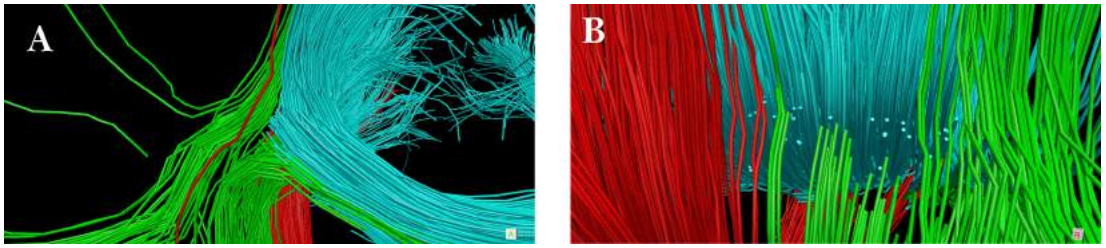

Figure 4.3: Misinterpreted DTI tracts. In cyan the CC tracts, red the CST tracts and in green the misinterpreted tracts. In panel A, in the crossing fibre region, the MDD misleads both lower CST tracts to become CC tracts (right-hand side green tracts) and upper CST tracts to become CC tracts (left-hand side green tracts). In panel B, the contribution of multiple fibre populations forces these voxels to have a FA value bellow the threshold for the algorithm, which then terminates the reconstruction.

4.2 Connectivity

4.2.1 Global Connectivity

Global connectivity analysis was performed on the mean of all 6 subjects, using complex network analysis and the visualization capabilities of MIBCA. Global adjacency matrices were acquired and, with them, connectograms were computed. In Figure 4.4 we can see a side-by-side comparison of two connectograms, the first for CLS-KT and the second one for NL-DTI. Both connectograms are limited by a minimum threshold of 0.8, i.e. 80% of the less relevant connections (considered spurious) were removed, and only the 20% most relevant connections remained. There is a clear distinction in the connectograms, particularly when looking at the central area of the connectogram. Connections that invade this area are inter-hemispherical. NL-DTI connectogram shows low numbers of inter-hemispherical connections when compared to the CLS-KT connectogram. This could be due to the fact that DKI has the ability to account for multiple fibres per voxel. In turn, commissural fibres tend to be better detected when crossing other fibres, and therefore, more inter-hemispherical connections are established. The counterpart is seen in Fig. 4.3, where commissural fibres are misinterpreted and detoured, leading to not establishing an inter-hemispherical connection.

Using the MIBCA environment it was also possible to perform operations between adjacency matrices. To understand the global differences in connections between the several tractographies, the adjacency matrices were subtracted in pairs of the form *DKI-DTI*. These connectograms showcase the exclusive connections between the two matrices.

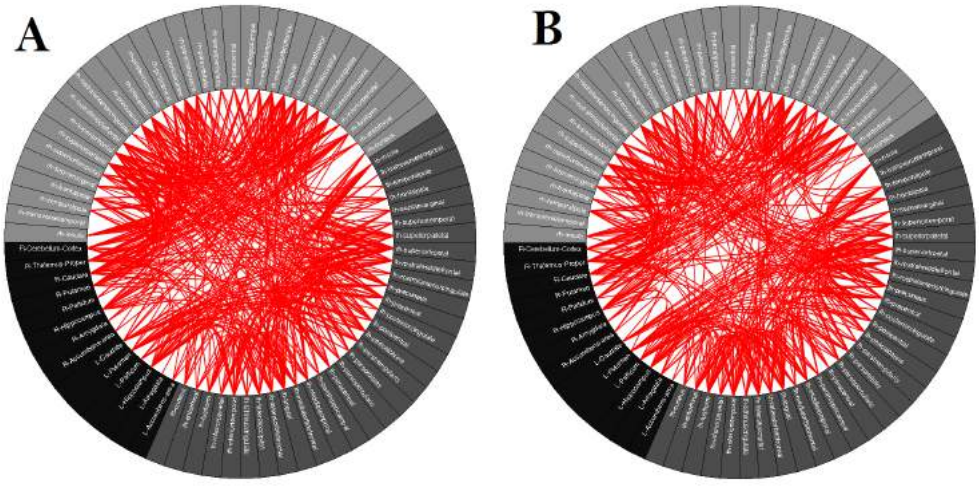

Figure 4.4: DKI and DTI based structural connectivity connectograms. Light grey areas correspond to right hemispherical cortical regions, dark grey areas to left hemispherical cortical regions and black areas to subcortical regions, both left and right. Panel A shows the CLS-KT based connectogram and panel B shows the NL-DTI based connectogram. The NL-DTI connectogram shows sparser connections in the middle of the connectogram, an indication of lower numbers of inter-hemispherical connections.

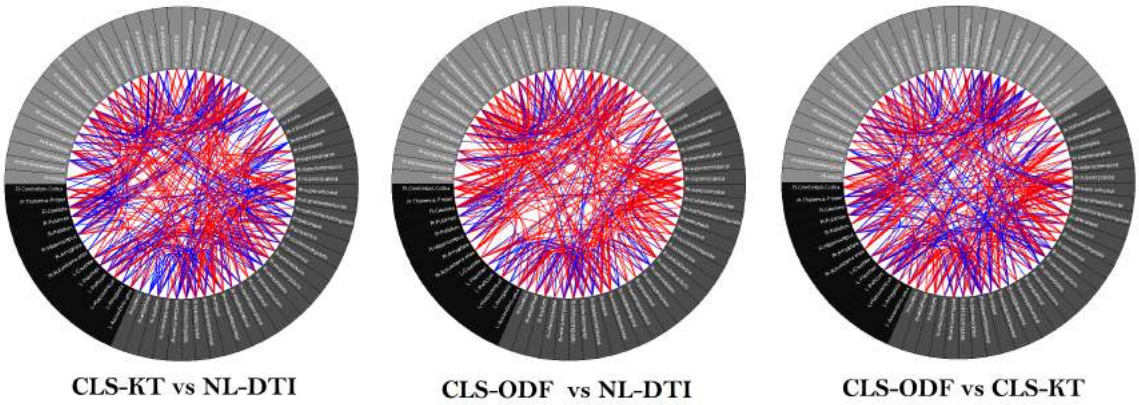

Figure 4.5: Difference connectograms, displaying connections exclusive to each method. The left connectogram displays exclusive connections to CLS-KT (red) and NL-DTI (blue). The middle connectogram shows exclusive connections to CLS-ODF (red) and NL-DTI (blue). The right connectogram exhibits the exclusive connections to CLS-ODF (red) and CLS-KT (blue). CLS-KT based connectograms seem to be less sensitive to intra-hemipherical connections, when compared to NL-DTI, but resolve many more inter-hemispherical connections. CLS-ODF outperforms NL-DTI in both intra and inter-hemispherical connections. When comparing CLS-ODF and CLS-KT, the first one seems to perform better with respect to intra-hemispherical connections whereas in inter-hemispherical connections both seem to resolve a great amount of connections. All connectograms were thresholded at 0.8 before the operation.

Examples of connectograms obtained from these difference matrices are shown in Figure 4.5.

From the difference of the connectograms in 4.4 (CLS-KT and NL-DTI), we can verify that CLS-KT based connectograms resolve more inter-hemispherical connections when compared to NL-DTI. This is seen by the predominance of red connections in the central area of the connectogram in Figure 4.5. Despite that, NL-DTI seems to show a greater amount of resolved intra-hemispherical connections, shown by the hemispherical concentration of blue connections. These results are not the same when comparing CLS-ODF and NL-DTI. CLS-ODF based connectograms appear to resolve not only more inter-hemispherical connections, but also, more intra-hemispherical connections, as seen in Fig. 4.5, by the overall predominance of red connections. When comparing the two DKI methods fitted with CLS, CLS-KT connectograms lack resolution in intra-hemispherical connections, but seem to resolve more inter-hemispherical connections. Overall, DKI-ODF methods not only reproduce but also expand on the NL-DTI connections, in both intra- and inter-hemispherical connections. The DKI-KT method only displays improvements in inter-hemispherical connections, but lacks resolution in intra-hemispherical connections, even when compared to NL-DTI.

The results are analogous when comparing DKI-OLS with NL-DTI and DKI-CLS with L-DTI.

The global connectivity metrics obtained for each tractography are shown in Table

4.1. Wilcoxon signed rank tests were also performed on the mean global connectivity metrics for each method (mean over subjects). The test was aimed at testing the hypothesis that the differences seen are statistically relevant, at 95% confidence level. The results show p-values greater than 0.05, which ruled out this hypothesis. This could mean that despite the greater number of connections resolved by DKI, the global network arrangement remains unchanged, when compared to DTI. Which may mean that in spite of the better resolution from DKI, DTI results are just as good and shouldn't be discarded. It is also possible that the amount of subjects scanned may not be enough to deal with inter-subject variability. Six subjects may not be a su fficiently large cohort to accentuate common features and mitigate the inter-subject variability, making it hard to draw strong conclusions. The metrics themselves may also lack reproducibility, i.e. the same subject, for different scans, may yield different metric values, using the same processing method. This introduces extra variability in the study of these metrics, thus making it hard or impossible to withdraw definitive conclusions from them. Methods to deal with these limitations are discussed in the next chapter.

4.2.2 Local Connectivity

The MIBCA environment also allows for a visualization of the modularity of the networks at hand, also under the form of connectograms. Although modularity is a global connectivity metric, the modular community of the network may yield additional insight on the local arrangement of the network. In Figure 4.6, the modularity of the networks from CLS-KT and NL-DTI is shown, for the whole network (no threshold). DTI-based connectograms show clusters with a distinct intra-hemispherical configuration, with clusters mostly within each hemisphere and very few connections spanning across both hemispheres inside the same cluster. DKI-based connectograms show an increased number of inter-hemispherical connections, with several clusters extending over both hemispheres, where left hemisphere nodes are linked to right hemisphere nodes from the same cluster. Moreover, to better indicate the degree of inter-, intra-, and inter-/intra-hemisphere connections per ROI, metric rings were added to the connectogram. These rings display the metric's value for each ROI. DKI-based connectograms showed less regions with only intra-hemisphere connections (labelled with white square in the inner rings), and whole cohort of ROI's exhibited higher ratios of inter-hemisphere connections, intra-hemisphere connections and also inter-to-intra connections, when comparing to DTI-based connectograms.

From each pair of fitting methods, 6 Bland-Altman plots were created, one for each subject. In Figure 4.7 are presented the Bland-Altman plots obtained when comparing AD from CLS-KT and NL-DT. The full cohort of the plots are available in Appendix C.

A tendency is clearly observed between all subjects: the difference of the metric between the two fit-methods grows with the growth of the mean. This tendency is a consequence of the fitting model used to estimate the DT. When using DTI to estimate the

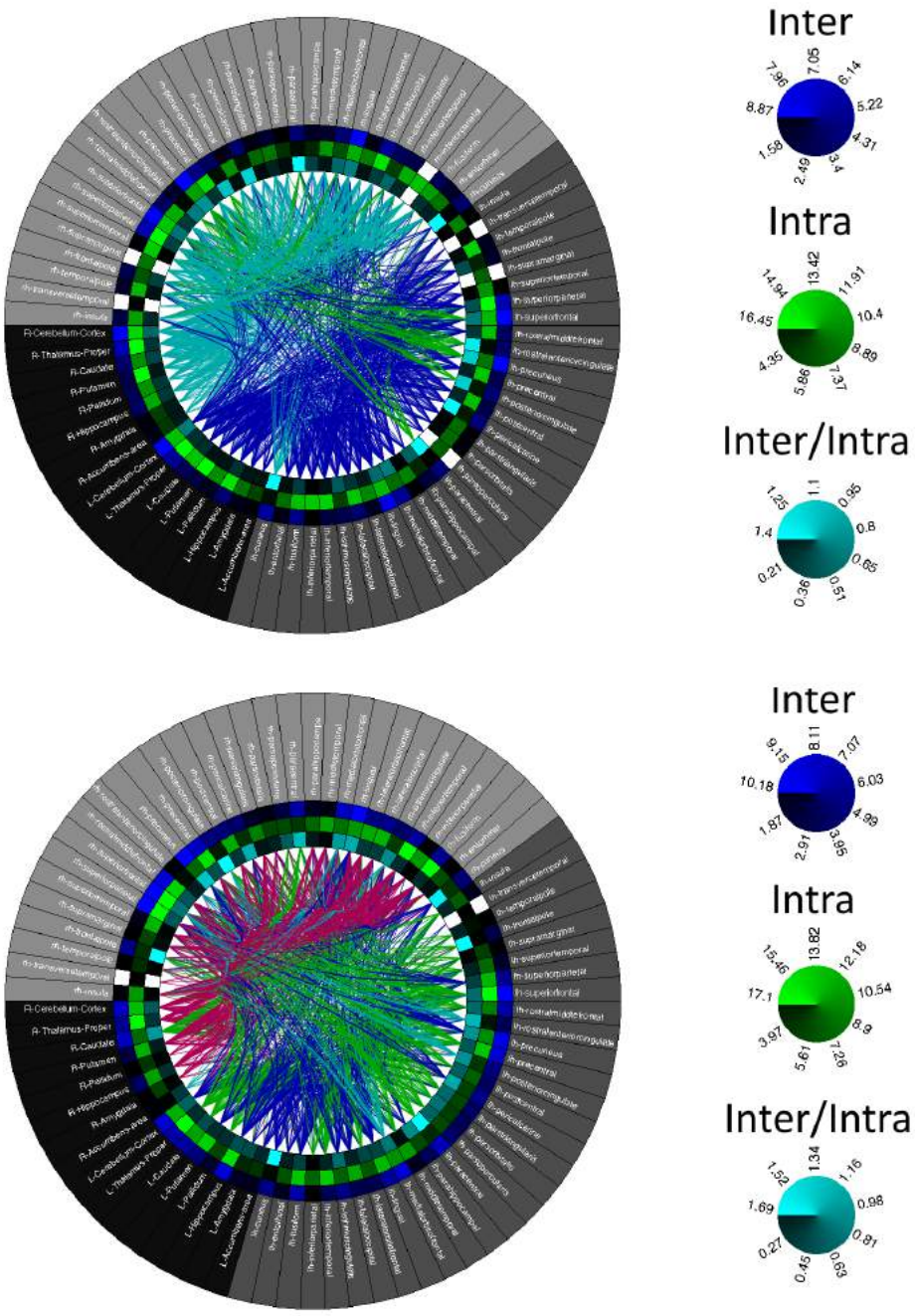

Figure 4.6: Modularity connectograms with metrics rings. The top connectogram displays the modularity for the NL-DTI full network (no threshold) and the bottom connectogram shows the modularity for the CLS-KT full network. NL-DTI modularity shows 3 clusters, with a clear intra-hemispheric configuration. On the other hand, CLS-KT network has 4 clusters, with multiple clusters spanning across both hemispheres. The inner rings represent the metrics on the right. The ROI's with white labelling in the ring correspond to regions with no inter-hemispheric connections. These are more frequent in the NL-DTI connectogram rather than in the CLS-KT one.

Subject	Tractography Method	Radius	Diameter	λ	Global Efficiency	Modularity	Small Wordlness
1	clsKT	5	10	3.41	0.34	0.22	5.77
	clsODF	4	6	3.07	0.36	0.25	4.56
	olsKT	6	12	3.48	0.34	0.22	5.57
	olsODF	8	14	3.27	0.36	0.25	4.43
	lDTI	5	10	3.12	0.37	0.26	5.12
	nlDTI	11	17	3.35	0.36	0.31	4.76
2	clsKT	4	8	3.23	0.35	0.22	5.97
	clsODF	4	6	3.07	0.37	0.20	4.87
	olsKT	5	9	3.03	0.37	0.19	5.26
	olsODF	4	7	2.98	0.38	0.21	4.63
	lDTI	5	9	2.98	3.38	0.20	4.98
	nlDTI	5	10	3.07	0.37	0.21	5.33
3	clsKT	40	56	4.76	0.31	0.23	5.49
	clsODF	9	17	3.80	0.32	0.26	5.09
	olsKT	4	11	3.33	0.35	0.21	6.20
	olsODF	5	10	3.28	0.36	0.24	5.56
	lDTI	5	9	3.30	0.35	0.22	6.79
	nlDTI	27	36	3.65	0.36	0.23	5.79
4	clsKT	5	9	3.39	0.34	0.20	6.42
	clsODF	6	11	3.22	0.36	0.24	4.36
	olsKT	5	8	3.26	0.35	0.23	6.75
	olsODF	4	7	3.10	0.36	0.23	4.36
	lDTI	5	8	3.26	0.35	0.24	6.88
	nlDTI	6	12	3.49	0.34	0.26	6.99
5	clsKT	7	14	3.69	0.33	0.27	5.23
	clsODF	5	9	3.34	0.34	0.29	4.63
	olsKT	5	10	3.32	0.35	0.25	5.89
	olsODF	10	16	3.34	0.36	0.27	4.33
	lDTI	4	7	2.92	0.38	0.23	5.63
	nlDTI	5	9	3.14	0.36	0.24	6.29
6	clsKT	5	7	3.35	0.34	0.28	5.18
	clsODF	10	16	3.57	0.34	0.24	4.50
	olsKT	5	9	3.47	0.33	0.24	6.14
	olsODF	7	13	3.39	0.34	0.25	4.86
	lDTI	5	10	3.40	0.34	0.22	5.65
	nlDTI	5	9	3.23	0.35	0.23	5.30

Table 4.1: Global connectivity metrics results for all tractography datasets performed for each subject.

DT, the non-Gaussian properties of diffusion are neglected, which leads to the estimation of an "apparent diffusion tensor", highly dependent of the b-value(s) used in the acquisition. Particularly, the higher the b-value used, the more underestimated this "apparent diffusion tensor" is. If one uses DKI to estimate the DT, the non-Gaussian properties are accounted into the DT, and the b-value dependencies are lifted [33]. Therefore, it is

expected that DKI estimated DT values are higher than that estimated by DTI. These differences are accentuated when the mean metrics values increase (x-axis in Bland-Altman plots), and thus, this tendency is created.

From these plots, significantly different ROI's were identified using the criteria a difference between the different fittings' metric above the *mean+2std* threshold (upper red line in Fig. 4.7). From these ROI's, systematically "flagged" ROI were identified ("flagged" for 50% or more of the subjects) and individually treated with regards to their connectivity metrics and their respective variation between tractography methods. The list of systematically "flagged" ROI is presented in Tables 4.2 and 4.3, as well as their respective metrics for each tractography. The regions in these tables are the regions "flagged" for all of the paired comparisons.

For CLS-DKI vs L-DTI, the "flagged" regions were ctx-rh-transversetemporal (when comparing AD and MD)and ctx-rh-entorhinal (for all 3 metrics). Taken into consideration these fittings CLS-DKI and L-DTI, CLS-KT, CLS-ODF and L-DTI are the tractography sets to compare.

In ctx-rh-entorhinal, CLS-KT-based tractography showed the lowest values for node degree, clustering coefficient, betweenness centrality, participation coefficient and local efficiency, and in eccentricity showed the highest values. CLS-ODF, on the other hand, showed the highest values for all of the first metrics, except for the participation coefficient, where L-DTI proved to have the highest of all three. In ctx-rh-transversetemporal,

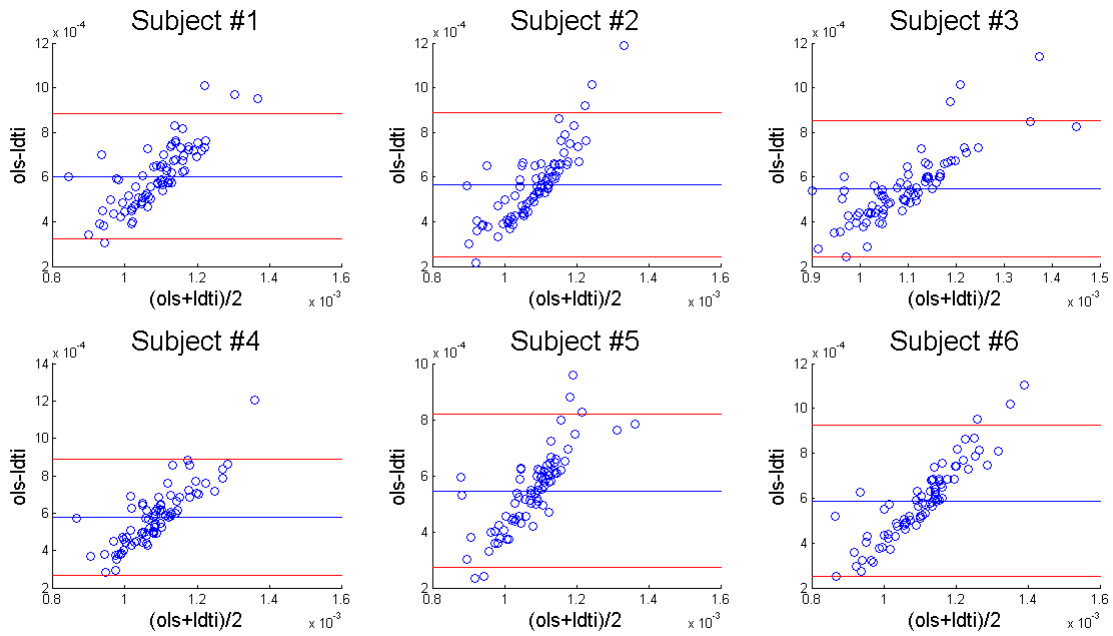

Figure 4.7: Bland-Altman plots of AD from CLS-KT and NL-DT. The blue line is the mean of the differences, and the red lines are ± 2std. All of the subjects display the same tendency: the difference of the metric increases with the increase of the mean of the metric.

ROI	Tractography Method	Node Degree	Clustering Coefficient	Eccentricity
ctx-lh-entorhinal	clsKT	25.3	6.8	12.2
	clsODF	29.5	8.8	8.0
	olsKT	25.3	7.3	6.3
	olsODF	33.3	8.6	8.5
	lDTI	31.3	5.8	6.2
	nlDTI	32.3	5.4	11.2
ctx-rh-entorhinal	clsKT	7.3	4.0	13.0
	clsODF	15.7	4.9	8.2
	olsKT	10.7	4.7	6.7
	olsODF	11.7	4.9	9.2
	lDTI	16.2	4.5	6.0
	nlDTI	15	3.6	12.0
ctx-rh-postcentral	clsKT	15.0	11.8	13.0
	clsODF	22.2	9.2	8.0
	olsKT	14.2	14.2	7.2
	olsODF	24.3	9.5	8.8
	lDTI	14.7	6.8	6.5
	nlDTI	16	7.5	12.5
ctx-rh-transversetemporal	clsKT	1.8	6.6	14.7
	clsODF	2.7	2.8	8.7
	olsKT	1.7	5.4	5.8
	olsODF	2.8	4.1	7.7
	lDTI	2.8	6.0	6.7
	nlDTI	1.2	1.3	8

Table 4.2: Systematically "flagged" ROI's from the Bland-Altman plots, with their respective connectivity metrics for each tractography.

CLS-KT-based tractography was shown to have the lowest node degree, betweenness centrality and participation coefficient. It has the highest local efficiency, clustering coefficient and eccentricity. CLS-ODF tractography showed the complete opposite of CLS-KT, except for betweenness centrality, while L-DTI showed the highest value in betweenness centrality and in between values for all o the other metrics.

When comparing CLS-DKI vs NL-DTI, ctx-rh-transversetemporal was "flagged" for all 3 metrics, and ctx-rh-postcentral was flagged for RD and MD. In this comparison, the tractography sets considered were CLS-KT, CLS-ODF and NL-DTI.

In the ctx-rh-transversetemporal, the connectivity metrics for NL-DTI yield values quite opposite to those presented before for the same region. NL-DTI tractography showed the lowest values for local efficiency, node degree and clustering coefficient. For betweenness centrality and participation coefficient, NL-DTI and CLS-KT were matched. CLS-KT had higher local efficiency, eccentricity and clustering coefficient, while CLS-ODF showed higher node degree, betweenness centrality and participation coe fficient. In the ctx-rh-postcentral region, the results were similar to the above for the transversetemporal

ROI	Tractography Method	Betweenness Centrality	Participation Coefficient	Local Efficiency
ctx-lh-entorhinal	clsKT	433.2	0.6	14.8
	clsODF	213.9	0.6	20.4
	olsKT	394.9	0.5	15.6
	olsODF	418.5	0.7	19.1
	lDTI	509.6	0.6	13.0
	nlDTI	445.0	0.5	12.5
ctx-rh-entorhinal	clsKT	104.7	0.3	6.3
	clsODF	221.6	0.5	9.6
	olsKT	310.6	0.3	7.8
	olsODF	106.5	0.5	8.4
	lDTI	177.0	0.6	8.6
	nlDTI	236.1	0.5	7.0
ctx-rh-postcentral	clsKT	132.7	0.6	20.5
	clsODF	190.5	0.6	19.8
	olsKT	156.5	0.5	22.2
	olsODF	114.2	0.6	20.9
	lDTI	217.7	0.4	12.8
	nlDTI	117.8	0.5	14.7
ctx-rh-transversetemporal	clsKT	0	0	7.9
	clsODF	7.6	0.2	3.7
	olsKT	1.33	0	6.3
	olsODF	12.1	0.2	5.0
	lDTI	16.1	0.1	6.6
	nlDTI	6.3	0	1.3

Table 4.3: Systematically "flagged" ROI's from the Bland-Altman plots, with their repective connectivity metrics for each tractography.

region, with the exception that betweenness centrality was higher for NL-DTI.

Moving on to OLS-DKI vs L-DTI, ctx-rh-entorhinal and ctx-lh-entorhinal were flagged, both for all 3 metrics. In this case, the tractographies considered were OLS-ODF, OLS-KT and L-DTI. Although homologous, the two regions displayed di fferences in both the metrics' range and tractography variation.

In ctx-lh-entorhinal, OLS-ODF displayed the highest values for node degree, clustering coefficient, eccentricity, participation coefficient and local efficiency. L-DTI tractography had the highest betweenness centrality. OLS-KT showed the lowest values for node degree, betweenness centrality and participation coefficient. In its counterpart area, clustering coefficients and eccentricity seen the same kind of variation for the 3 tractographies. L-DTI had the highest node degree, participation coefficient and local efficiency. OLS-KT tractography had the highest betweenness centrality.

Finally, OLS-DKI vs NL-DTI "flagged" ctx-rh-transversetemporal and ctx-rh-entorhinal for all 3 metrics and ctx-lh-entorhinal for AD and MD. The tractographies considered were then OLS-KT, OLS-ODF and NL-DTI.

In the ctx-lh-entorhinal region, NL-DTI showed the highest eccentricity and betweenness centrality and the lowest clustering coefficient. In terms of participation coefficient, CLS-KT and NL-DTI are up to par, but OLS-ODF displays the highest value. OLS-ODF also displays the highest value of local e fficiency, node degree and clustering coe fficient. In the ctx-rh-entorhinal region, OLS-ODF shows similar comparative results as in the previous region, except for node degree, where NL-DTI displays the highest value. NL-DTI also shows higher eccentricity, but in terms of betweenness centrality OLS-KT tractography exhibits a higher value. As for the ctx-rh-transversetemporal region, OLS-ODF displays higher values of node degree, betweenness centrality and participation coefficient. OLS-KT has the highest local efficiency and clustering coefficient. NL-DTI shows the highest value of eccentricity of the three.

The overall local connectivity metrics scenario seems to point out to a better characterization of the brain network using DKI-based tractography, with an overall highest local efficiency and participation coefficient. This may be a consequence of the crossing fibres extra sensitivity, not only for inter-hemispherical connections but also for intra-hemisphere connections, in the sense that regions with these crossing fibres bundles would have a higher participation coefficient (more paths in which they partake) and therefore a higher local efficiency. To note that one of the flagged regions, ctx-rh-transversetemporal, does not display inter-hemispherical connections. This further supports the notion that the DKI-based networks improve on the intra-hemispherical connections computed, when compared to those of DTI-based networks.

Despite that, local connectivity metrics are subject of great variation. Just like global metrics, local connectivity metrics variation can be subject of lack of reproducibility, linked to intra-subject variability, and to the effect size of the cohort, and could also be accountable for erroneous conclusions.

Chapter 5

Conclusions and Future Work

In this chapter, the conclusions of this dissertation will be presented, along with final considerations on the overall dissertation and possible future endeavours.

In this work we proposed a novel approach to study brain structural connectivity, based on DKI. The novelty factor in this work resulted in an increased degree of difficulty in both determining the path to perform the analysis and the validation of the results.

The dissertation turned around the comparison of the results obtained from DTI and DKI, in an effort to assess which technique stands out as the better one for brain network characterization. To accomplish this, two paths of analyses were followed, a tractography analysis and complex network analysis.

As expected, DTI-based tractography sets failed to resolve crossing fibres between the CST and the CC. This resulted in a lower amount of CC tracts isolated for either of the DTI tractography sets.

DKI-based tractography showed increased sensibility to fibre crossing regions between CST and CC and consequently an increased amount of computed CC tracts, occupied voxels and volume per structure. Although, DKI-KT method systematically showed a lower amount of computed CST tracts. This may be a consequence of the KT method of fibre tracking to the multi-compartmental parameters. This translates into a lower capability of tracking along long several regions of the brain. Since CST tracts run across the whole brain, it is expected that fibre tracking is undermined. DKI-ODF method didn't show this limitation.

For future studies, encompassing into the tractography study more fibre tracts, rather than just CST and CC, should help provide a more comprehensive analysis of the performance of DKI-based reconstruction throughout the whole brain.

The connectivity study was branched into two. The first was aimed at determining differences between DTI- and DKI-based connectograms at a global level, while also

looking at the global connectivity metrics obtained from the several networks.

Difference connectograms between DKI and DTI networks were computed to directly compare pairs of networks. These showed an increased amount of inter-hemispherical connections resolved by the DKI-based networks when compared to those of DTI. This can be a direct consequence of the crossing fibres detection possible with DKI, since it is more sensitive to commissural fibres, which tend to cross several other structures. DTI-based connectograms were shown to better identify intra-hemispherical connections when compared to the KT model, whereas the DKI-ODF model out performed the DTI model for intra-hemispherical connections. This lead to the notion that DKI-ODF not only detects the same connections as DTI, but also improves on them, resolving additional connections.

Modularity connectograms were also computed. In these the community structure of the network was assessed. DTI-based connectograms show a clear intra-hemispherical configuration of modules, with 3 clusters, where 2 are mainly responsible for establishing intra-hemispherical connections, and the third one is mostly responsible for some inter-hemispherical connections. DKI-based connectograms show an increased number of clusters and inter-hemispherical connections inside each cluster.

Inter-hemisphere, intra-hemisphere and inter-to-intra-hemisphere ratios were also computed. DTI-based networks showed more nodes with only intra-hemispherical connections, compared to DKI ones. Moreover, DKI-based networks show higher values for each of the three ratios.

Global and local connectivity metrics were obtained through complex network analysis.

Global connectivity metrics show some variation between tractography methods for each subject. Looking for statistical validity, the means of the metrics for each tractography were calculated, across the 6 subjects, and then two-sided Wilcoxon tests were performed in pairs of networks in the form DKIvsDTI. These tests revealed that the DKI and DTI metrics are not statistically distinct. This leads to the notion that intra-subject variability may affect the outputs of complex network analysis, and therefore no assumptions can be made on the matter of which method characterizes connectivity better.

Local connectivity metrics were used on ROI identified by significant changes in the diffusion metrics, in an effort to establish a bridge between diffusion metrics variation and local connectivity metrics variation, for both tensors, and all 4 tensor fittings (L-DT, NL-DT, OLS-KT, CLS-KT). Systematically "flagged" ROI's were analysed for connectivity metrics variations, based on the threshold of *mean+2*std*. Overall, DKI-based networks seem to have higher local efficiency and participation coefficient, a consequence of the heightened sensitivity to crossing fibres, which in turn resolves better This translates into what could be a better characterization of the human brain network, thought to have highly efficient nodes, participating in a high number of inter-cluster connections. This characterization could also be closer to the ground-truth. However, local connectivity metrics are also subject to quite some variability. The origin of this variability could be

and the conclusions withdrawn from them can be erroneous.

Overall, the objectives of this dissertation were partially met. In the sense that tractography and structural connectivity study goals were met, but establishing a clear connection between diffusion metrics and connectivity metrics was not possible.

As a final conclusion, DKI-based networks seem to have additional insight in the characterization of the human brain networks, but the full extent of these insights is yet to be determined.

To try and mitigate the shortcomings of this dissertation, an improvement to this work would be to consider a larger cohort of subjects, since a dataset of 6 subjects may not have the statistical power necessary to draw strong conclusions. Also, consider a test/re-test procedure for data acquisition. This way, it would possible to test for metric reproducibility intra-subject and understand if the differences seen in the connectivity metrics are or not a result of this variability. Furthermore, to expand the diffusion metrics relationship to the connectivity metrics, a study using confidence ellipsoids instead of a simple *mean+2*std* threshold could be performed, studying all of the ROI that are placed outside the confidence ellipsoid

Bibliography

[1] P. C. Lauterbur. "Image Formation by Induced Local Interactions: Examples Employing Nuclear Magnetic Resonance". In: *Nature* 242 (1973), pp. 190–191.

[2] W. Longstreth, T. A. Manolio, A. Arnold, G. L. Burke, N. Bryan, C. A. Jungreis, P. L. Enright, D. O'Leary, and L. Fried. "Clinical Correlates of White Matter Findings on Cranial Magnetic Resonance Imaging of 3301 Elderly People: The Cardiovascular Health Study". In: *Stroke* 27.8 (1996), pp. 1274–1282.

[3] I. V. Allen and S. R. McKeown. "A histological, histochemical and biochemical study of the macroscopically normal white matter in multiple sclerosis". In: *J Neurol Sci* 41.1 (1979), pp. 81–91.

[4] T. Baumgartner, K. Nash, C. Hill, and D. Knoch. "Neuroanatomy of intergroup bias: A white matter microstructure study of individual differences". In: *NeuroImage* 122 (2015), pp. 345–354.

[5] A. L. Murray, D. K. Thompson, L. Pascoe, A. Leemans, T. E. Inder, L. W. Doyle, J. F. Anderson, and P. J. Anderson. "White matter abnormalities and impaired attention abilities in children born very preterm". In: *NeuroImage* 124 (2016), pp. 75–84.

[6] T. E. Conturo, N. F. Lori, T. S. Cull, E Akbudak, a. Z. Snyder, J. S. Shimony, R. C. McKinstry, H Burton, and M. E. Raichle. "Tracking neuronal fiber pathways in the living human brain." In: *Proceedings of the National Academy of Sciences of the United States of America* 96.August (1999), pp. 10422–10427.

[7] P. J. Basser, S. Pajevic, C. Pierpaoli, J. Duda, and A. Aldroubi. "In vivo fiber tractography using DT-MRI data". In: *Magnetic Resonance in Medicine* 44 (2000), pp. 625–632.

[8] D. Tuch, T. Reese, M. Wiegell, N Makris, J. Belliveau, and V. Wedeen. "High angular resolution diffusion imaging reveals intravoxel white matter fiber heterogeneity". In: *NeuroImage* 23 (2002), pp. 1176–1185.

[9] T. E. J. Behrens, M. W. Woolrich, M Jenkinson, H Johansen-Berg, R. G. Nunes, S Clare, P. M. Matthews, J. M. Brady, and S. M. Smith. "Characterization and propagation of uncertainty in diffusion-weighted MR imaging." In: *Magnetic resonance in medicine : official journal of the Society of Magnetic Resonance in Medicine / Society of Magnetic Resonance in Medicine* 50.5 (2003), pp. 1077–88.

[10] Y. Iturria-Medina, R. C. Sotero, E. J. Canales-Rodríguez, Y. Alemán-Gómez, and L. Melie-García. "Studying the human brain anatomical network via diffusion-weighted MRI and Graph Theory". In: *NeuroImage* 40 (2008), pp. 1064–1076.

[11] M. H. a. Bauer, D. Kuhnt, S. Barbieri, J. Klein, A. Becker, B. Freisleben, H. K. Hahn, and C. Nimsky. "Reconstruction of White Matter Tracts via Repeated Deterministic Streamline Tracking - Initial Experience". In: *PLoS ONE* 8.5 (2013).

[12] S. Mori and J. Zhang. "Principles of Diffusion Tensor Imaging and Its Applications to Basic Neuroscience Research". In: *Neuron* 51.5 (2006), pp. 527–539.

[13] J. I. Berman, M. S. Berger, P. Mukherjee, and R. G. Henry. "Diffusion-tensor imaging-guided tracking of fibers of the pyramidal tract combined with intraoperative cortical stimulation mapping in patients with gliomas." In: *Journal of neurosurgery* 101.1 (2004), pp. 66–72.

[14] D. K. Jones. "Challenges and limitations of quantifying brain connectivity in vivo with diffusion MRI". In: *Future Medicine* 2.3 (2010), pp. 341–355.

[15] D. K. Jones, T. R. Knösche, and R. Turner. "White matter integrity, fiber count, and other fallacies: The do's and don'ts of diffusion MRI". In: *NeuroImage* 73 (2013), pp. 239–254.

[16] D. S. Tuch. "Q-ball imaging". In: *Magnetic Resonance in Medicine* 52.6 (2004), pp. 1358–1372.

[17] V. Wedeen, R. Wang, J. Schmahmann, T. Benner, W. Tseng, G. Dai, D. Pandya, P. Hagmann, H. D'Arceuil, and A. de Crespigny. "Diffusion spectrum magnetic resonance imaging (DSI) tractography of crossing fibers". In: *NeuroImage* 41.4 (2008), pp. 1267–1277.

[18] A. L. Alexander, Y.-C. Wu, and P. C. Venkat. "Hybrid diffusion imaging (HYDI)." In: *Conference proceedings : ... Annual International Conference of the IEEE Engineering in Medicine and Biology Society. IEEE Engineering in Medicine and Biology Society. Conference* 1 (2006), pp. 2245–8.

[19] J. a. Helpern, V. Adisetiyo, M. F. Falangola, C. Hu, A. Di Martino, K. Williams, F. X. Castellanos, and J. H. Jensen. "Preliminary Evidence of Altered Gray and White Matter Microstructural Development in the Frontal Lobe of Adolescents with Attention-Deficit Hyperactivity Disorder: A Di ffusional Kurtosis Imaging Study". In: *Journal of magnetic resonance imaging : JMRI* 33.1 (2011), pp. 17–23.

[20] J.-D. Tournier, F. Calamante, and A. Connelly. "Robust determination of the fibre orientation distribution in diffusion MRI: Non-negativity constrained super-resolved spherical deconvolution". In: *NeuroImage* 35.4 (2007), pp. 1459–1472.

[21] T. E. J. Behrens, H. J. Berg, S. Jbabdi, M. F. S. Rushworth, and M. W. Woolrich. "Probabilistic diffusion tractography with multiple fibre orientations: What can we gain?" In: *NeuroImage* 34 (2007), pp. 144–155.

[22] P. Fillard, C. Poupon, and J.-F. Mangin. "A novel global tractography algorithm based on an adaptive spin glass model." In: *International Conference on Medical Image Computing and Computer Assisted Intervention (MICCAI'09)* 12.Pt 1 (2009), pp. 927–34.

[23] P. Fillard, M. Descoteaux, A. Goh, S. Gouttard, B. Jeurissen, J. Malcolm, A. Ramirez-Manzanares, M. Reisert, K. Sakaie, F. Tensaouti, T. Yo, J. F. Mangin, and C. Poupon. "Quantitative evaluation of 10 tractography algorithms on a realistic diffusion MR phantom". In: *NeuroImage* 56.1 (2011), pp. 220–234.

[24] L. Zhan, J. Zhou, Y. Wang, Y. Jin, N. Jahanshad, G. Prasad, T. M. Nir, and C. D. Leonardo. "Comparison of 9 Tractography Algorithms for Detecting Abnormal Structural Brain Networks in Alzheimer ' s Disease Comparison of 9 Tractography Algorithms for Detecting Abnormal Structural Brain Networks in Alzheimer ' s Disease". In: *Frontiers in Aging Neuroscience* 7.April (2015), pp. 1–19.

[25] H.-W. Chung, M.-C. Chou, and C.-Y. Chen. "Principles and Limitations of Computational Algorithms in Clinical Diffusion Tensor MR Tractography". In: *American Journal of Neuroradiology* 32 (2010), pp. 3–13.

[26] C. P. Lin, V. J. Wedeen, J. H. Chen, C. Yao, and W. Y. I. Tseng. "Validation of diffusion spectrum magnetic resonance imaging with manganese-enhanced rat optic tracts and ex vivo phantoms". In: *NeuroImage* 19.3 (2003), pp. 482–495.

[27] P. Raab, E. Hattingen, K. Franz, F. E. Zanella, and H. Lanfermann. "Cerebral gliomas: diffusional kurtosis imaging analysis of microstructural differences." In: *Radiology* 254.3 (2010), pp. 876–881.

[28] K. Kamagata, H. Tomiyama, Y. Motoi, M. Kano, O. Abe, K. Ito, K. Shimoji, M. Suzuki, M. Hori, A. Nakanishi, R. Kuwatsuru, K. Sasai, S. Aoki, and N. Hattori. "Diffusional kurtosis imaging of cingulate fibers in Parkinson disease: Comparison with conventional diffusion tensor imaging". In: *Magnetic Resonance Imaging* 31.9 (2013), pp. 1501–1506.

[29] J. Zhu, C. Zhuo, W. Qin, D. Wang, X. Ma, Y. Zhou, and C. Yu. "Performances of diffusion kurtosis imaging and diffusion tensor imaging in detecting white matter abnormality in schizophrenia". In: *NeuroImage: Clinical* 7 (2015), pp. 170–176.

[30] C. Y. Lee, A. Tabesh, T. Nesland, J. H. Jensen, A Helpern, M. V. Spampinato, and L. Bonilha. "Human brain asymmetry in microstructural connectivity demonstrated by diffusional kurtosis imaging". In: *Brain Research* 1588 (2014), pp. 73–80.

[31] S. Chiang, J. M. Stern, J. Engel, H. S. Levin, and Z. Haneef. "Differences in graph theory functional connectivity in left and right temporal lobe epilepsy". In: *Epilepsy Research* 108.10 (2014), pp. 1770–1781.

[32] S Umesh Rudrapatna, T. Wieloch, K. Beirup, K. Ruscher, W. Mol, P. Yanev, A. Leemans, A. van der Toorn, and R. M. Dijkhuizen. "Can diffusion kurtosis imaging improve the sensitivity and specificity of detecting microstructural alterations in brain tissue chronically after experimental stroke? Comparisons with diffusion tensor imaging and histology." In: *NeuroImage* 97 (Aug. 2014), pp. 363–73.

[33] R. Neto-Henriques. "Diffusion Kurtosis Imaging of the Healthy Human Brain". PhD thesis. Universidade de Lisboa, 2012, p. 150.

[34] M. F. Falangola, J. H. Jensen, A. Tabesh, C. Hu, R. L. Deardorff, J. S. Babb, S. Ferris, and J. a. Helpern. "Non-Gaussian diffusion MRI assessment of brain microstructure in mild cognitive impairment and Alzheimer's disease". In: *Magnetic Resonance Imaging* 31.6 (2013), pp. 840–846.

[35] D. W. McRobbie, E. A. Moore, M. J. Graves, and M. R. Prince. *MRI: From Picture to Proton*, vol. 85. 2003, pp. 504–505.

[36] A. Einstein. "Investigations on the Theory of Brownian Movement". In: *New York Dover* (1956).

[37] D Le Bihan, E. Breton, D Lallemand, P Grenier, E Cabanis, and M Laval-Jeantet. "MR imaging of intravoxel incoherent motions: application to diffusion and perfusion in neurologic disorders." In: *Radiology* 161 (1986), pp. 401–407.

[38] E. O. Stejskal and J. E. Tanner. "Spin diffusion measurements: spin echoes in the presence of a time-dependant field gradient". In: *The Journal of chemical physics* 42 (1965), p. 5.

[39] I. Drobnjak, G. Zhang, A. Ianus, E. Kaden, and D. Alexander. "Maximising potential of axon diameter mapping using low frequency OGSE : Insight from simulation". In: *Organization for Human Brain Mapping 2015*. Honolulu, Hawaii: OHBM, 2015.

[40] P. J. Basser, J Mattiello, and D LeBihan. "Estimation of the effective self-diffusion tensor from the NMR spin echo." In: *Journal of magnetic resonance. Series B* 103 (1994), pp. 247–254.

[41] D. Le Bihan, J. F. Mangin, C. Poupon, C. A. Clark, S. Pappata, N. Molko, and H. Chabriat. "Diffusion tensor imaging: concepts and applications." In: *Journal of magnetic resonance imaging : JMRI* 13 (2001), pp. 534–546.

[42] M. Niethammer, R. San, and J. Estepar. "NIH Public Access". In: *IEEE Engineering in Medicine and Biology Magazine* 1 (2009), pp. 2622–2625.

[43] P Mukherjee, J. I. Berman, S. W. Chung, C. P. Hess, and R. G. Henry. "Diffusion tensor MR imaging and fiber tractography: theoretic underpinnings." In: *AJNR. American journal of neuroradiology* 29.4 (Apr. 2008), pp. 632–41.

[44] C. Pierpaoli and P. J. Basser. "Toward a Quantitative Assessment of Diffusion Anisotropy". In: *Magnetic Resonance in Medicine* 36.6 (1996), pp. 893–906.

[45] P. J. Basser. "Inferring Microstructural Features and the Physiological State of Tissues from Diffusion-Weighted Images". In: *NMR in Biomedicine* 8 (1995), pp. 333–344.

[46] J. H. Jensen and J. a. Helpern. "Diffusional kurtosis imaging: the quantification of non-gaussian water diffusion by means of magnetic resonance imaging". In: *Magnetic Resonance in Medicine* 53.6 (2005), pp. 1432–40.

[47] E. Wu and M. M. Cheung. "MR diffusion kurtosis imaging for neural tissue characterization". In: *NMR in Biomedicine* 23.7 (2010), pp. 836–48.

[48] P. Hagmann, L. Jonasson, P. Maeder, J.-p. Thiran, V. J. Wedeen, and R. Meuli. "Central Nervous System: State of the art Understanding Diffusion MR Imaging Techniques : From Scalar Imaging to Di ffusion". In: *RadioGraphics* 26 (2006), pp. 205–224.

[49] H. Lu, J. H. Jensen, A. Ramani, and J. a. Helpern. "Three-dimensional characterization of non-gaussian water diffusion in humans using diffusion kurtosis imaging". In: *NMR in Biomedicine* 19.2 (2006), pp. 236–247.

[50] E. S. Hui, M. M. Cheung, L. Qi, and E. X. Wu. "Towards better MR characterization of neural tissues using directional di ffusion kurtosis analysis". In: *NeuroImage* 42 (2008), pp. 122–134.

[51] R. Neto-Henriques, M. M. Correia, R. G. Nunes, and H. A. Ferreira. "Exploring the 3D geometry of the diffusion kurtosis tensor—Impact on the development of robust tractography procedures and novel biomarkers". In: *NeuroImage* 111 (2015), pp. 85–99.

[52] S. Jbabdi, M. W. Woolrich, J. L. R. Andersson, and T. E. J. Behrens. "A Bayesian framework for global tractography". In: *NeuroImage* 37.1 (2007), pp. 116–129.

[53] D. K. Jones. "Studying connections in the living human brain with diffusion MRI". In: *Cortex* 44 (2008), pp. 936–952.

[54] M. Lazar, J. H. Jensen, L. Xuan, and J. a. Helpern. "Estimation of the Orientation Distribuition Function from Diffusional Kurtosis Imaging". In: *Magn Reson Med* 60.4 (2008), pp. 774–781.

[55] M. Lazar. "Mapping brain anatomical connectivity using white matter tractography". In: *NMR in Biomedicine* 23.7 (2010), pp. 821–835.

[56] S. Mori and P. C. M. Van Zijl. "Fiber tracking: Principles and strategies - A technical review". In: *NMR in Biomedicine* 15.7-8 (2002), pp. 468–480.

[57] J. H. Jensen, J. A. Helpern, and A. Tabesh. "Leading non-Gaussian corrections for diffusion orientation distribution function". In: *NMR in Biomedicine* 27.2 (2014), pp. 202–211.

[58] M. Rubinov and O. Sporns. "Complex network measures of brain connectivity: Uses and interpretations". In: *NeuroImage* 52.3 (2010), pp. 1059–1069.

[59] O. Sporns and R. Kötter. "Motifs in Brain Networks". In: *PLoS Biology* 2(11):e369 (2004).

[60] O. Sporns. *Networks of the Brain*. 1st. Cambridge: MIT press, 2011, pp. 5–126.

[61] P. Hagmann, L. Cammoun, X. Gigandet, R. Meuli, C. J. Honey, J. Van Wedeen, and O. Sporns. "Mapping the structural core of human cerebral cortex". In: *PLoS Biology* 6.7 (2008), pp. 1479–1493.

[62] A. Ribeiro, L Lacerda, J Rodrigues, J. Sousa, and H. Ferreira. "Multimodal Imaging Brain Connectivity Analysis". In: *PeerJ* (2013), 3:e1078.

[63] R. Neto-Henriques, H. Ferreira, and M. Correia. "United Di ffusion Kurtosis Imaging toolbox". In: *ESMRMB 2015, 32nd Annual Scientific Meeting, Edinburgh, UK, 1-3 October: EPOS™ Poster / Paper Poster / Clinical Review Poster / Software Exhibits*. Vol. 28. S1. 2015, S512–S513.

[64] R. S. Desikan, F. Ségonne, B. Fischl, B. T. Quinn, B. C. Dickerson, D. Blacker, R. L. Buckner, A. M. Dale, R. P. Maguire, B. T. Hyman, M. S. Albert, and R. J. Killiany. "An automated labeling system for subdividing the human cerebral cortex on MRI scans into gyral based regions of interest". In: *NeuroImage* 31.3 (2006), pp. 968–980.

[65] M. Jenkinson, C. F. Beckmann, T. E. J. Behrens, M. W. Woolrich, and S. M. Smith. "Fsl". In: *NeuroImage* 62.2 (2012), pp. 782–790.

[66] H. Huang, J. Zhang, P. C. van Zijl, and S. Mori. "Analysis of noise effects on DTI-based tractography using the brute-force and multi-ROI approach". In: *Magnetic Resonance in Medicine* 52.3 (2004), pp. 559–565.

[67] M Catani and M. T. de Schotten. *Atlas of Human Brain Connections*. OUP Oxford, 2012, pp. 75–238.

[68] J. M. Bland and D. G. Altman. "Statistical Methods for Assessing Agreement Between Two Methods of Clinical Measurement". In: *The Lancet* (1986), pp. 307–310.

Appendix 1 - ROI List

	ROI
Sub-cortical	Cerebellum-Cortex
	Thalamus-Proper
	Caudate
	Putamen
	Pallidum
	Hippocampus
	Amygdala
	Accumbens-area
Cortical	Cuneus
	Entorhinal
	Fusiform
	Inferior-parietal
	Inferior-temporal
	Isthmus-cingulate
	Lateral-occipital
	Lateral-orbito-frontal
	Lingual
	Medial-orbito-frontal
	Middle-temporal
	Para-hippocampal
	Para-central
	Parsopercularis
	Parsorbitalis
	Parstriangularis
	Pericalcarine
	Post-central
	Posterior-cingulate
	Pre-central
	Pre-cuneus
	Rostral-anterior-cingulate
	Rostral-middle-frontal
	Superior-frontal
	Superior-parietal
	Superior-temporal
	Supra-marginal
	Frontal pole
	Temporal pole
	Transversetemporal
	Insula

Table A.1: Considered ROI List. This list encompasses 76 brain regions, of which, 8 are sub-cortical and 30 are cortical regions

Appendix B

Appendix 2 - Tractography results

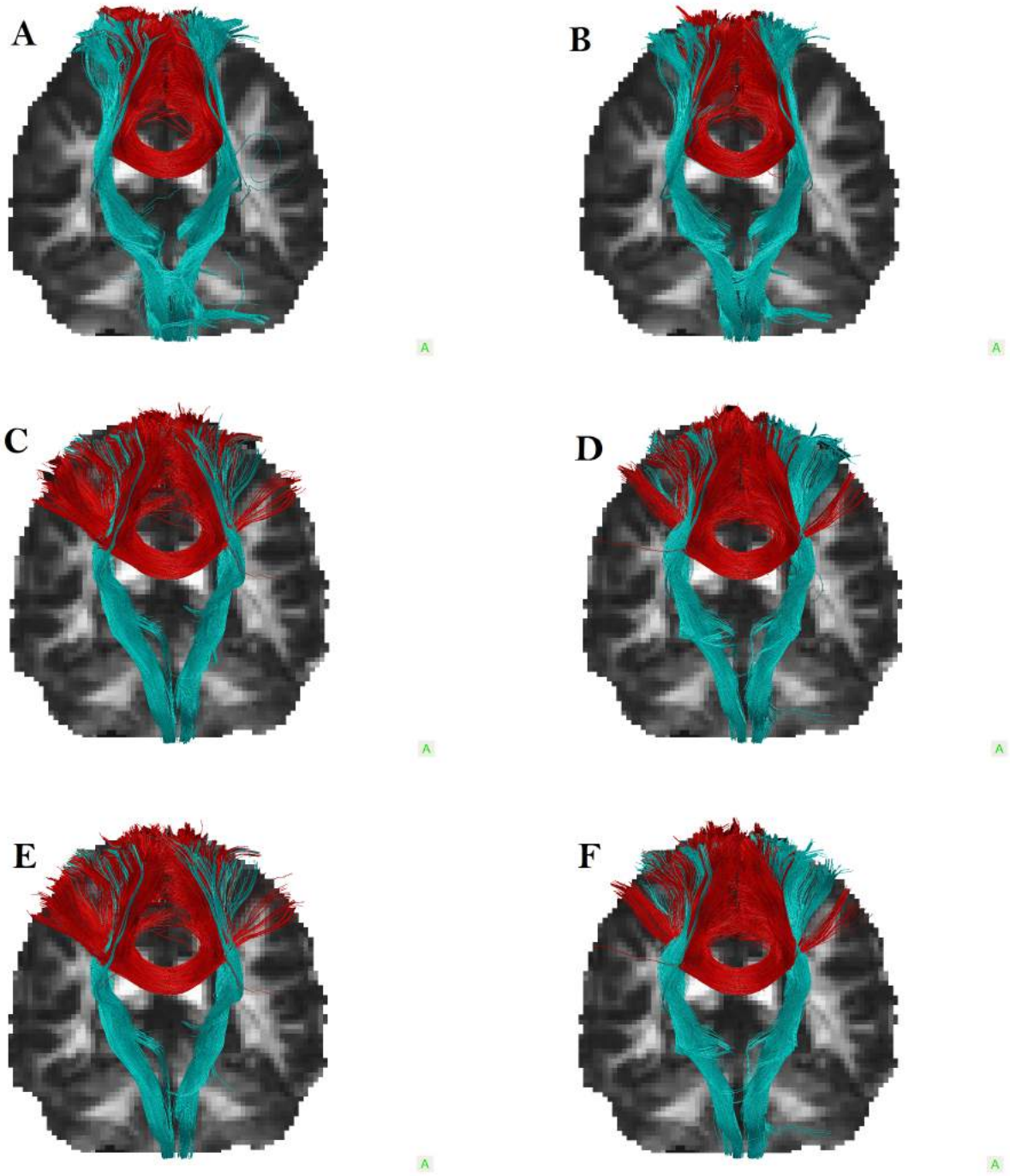

Figure B.1: Tractography reconstructions for subject 1. In cyan the CST tracts, red the CC tracts. In panels A and B, the L-DT and nL-DT reconstructions, respectively; panels B and C show the results for the OLS-KT and OLS-ODF; and panels D and E show the tractography results for CLS-KT and CLS-ODF reconstruction

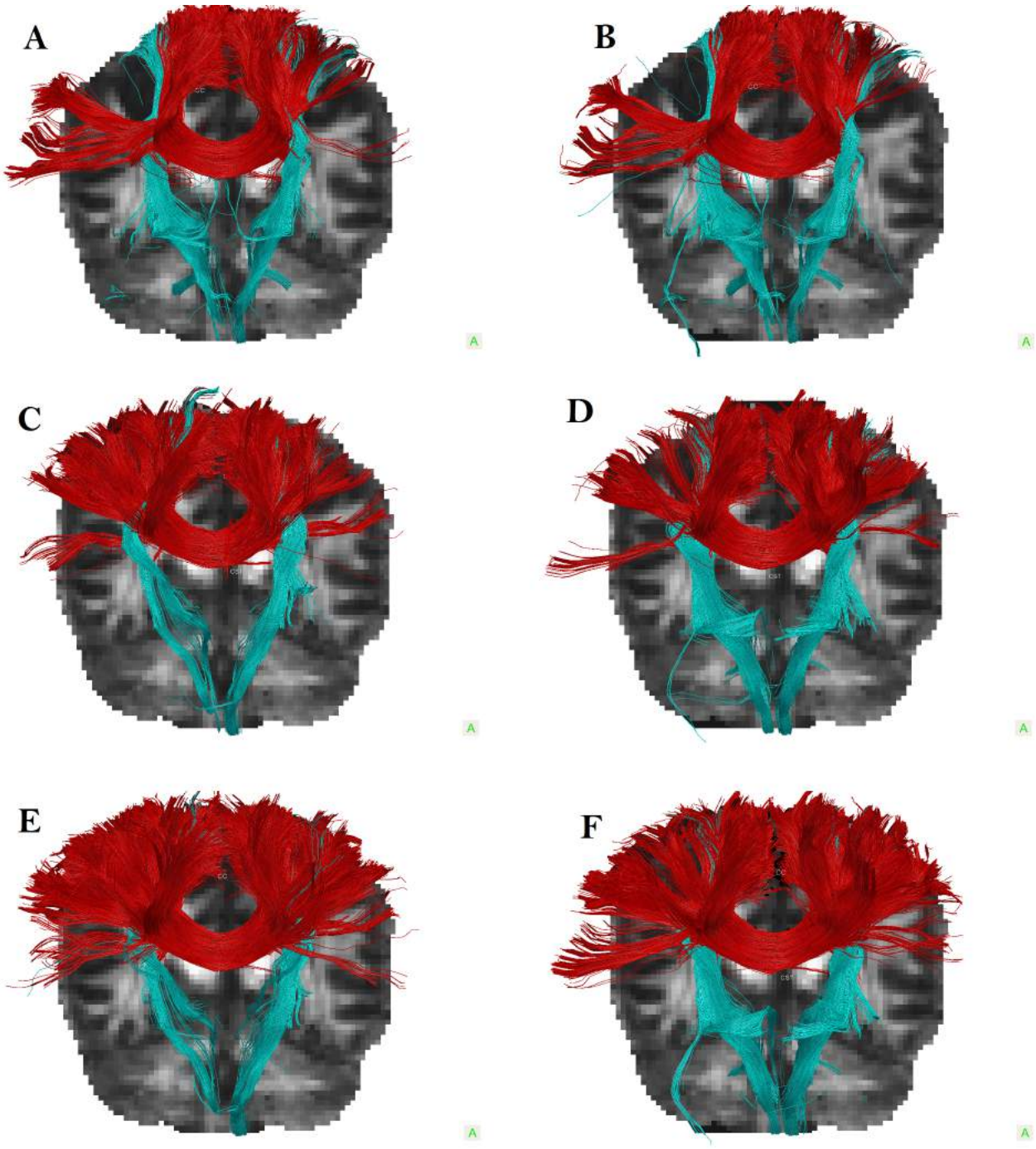

Figure B.2: Tractography reconstructions for subject 2. In cyan the CST tracts, red the CC tracts. In panels A and B, the L-DT and nL-DT reconstructions, respectively; panels B and C show the results for the OLS-KT and OLS-ODF; and panels D and E show the tractography results for CLS-KT and CLS-ODF reconstruction

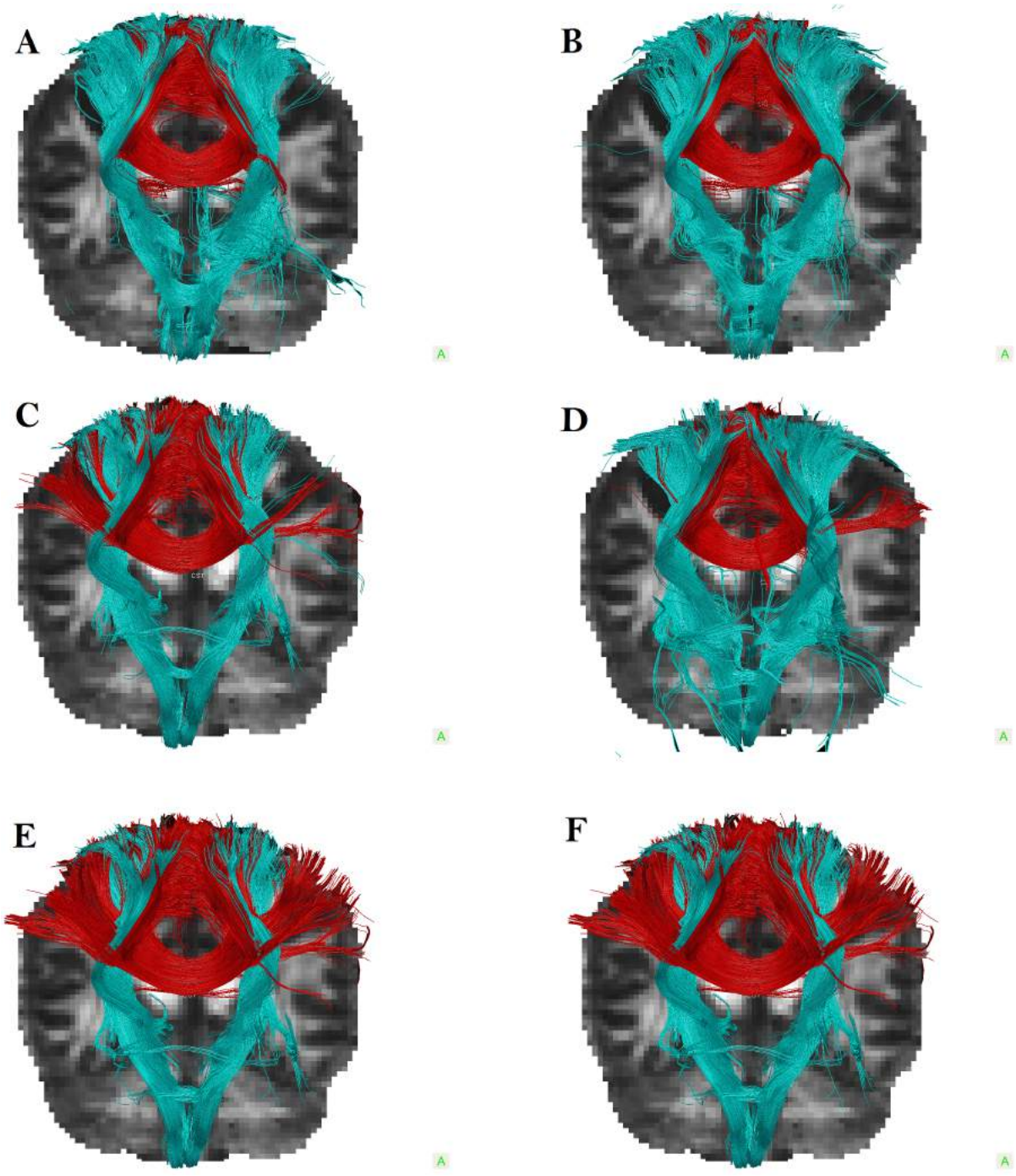

Figure B.3: Tractography reconstructions for subject 3. In cyan the CST tracts, red the CC tracts. In panels A and B, the L-DT and nL-DT reconstructions, respectively; panels B and C show the results for the OLS-KT and OLS-ODF; and panels D and E show the tractography results for CLS-KT and CLS-ODF reconstruction

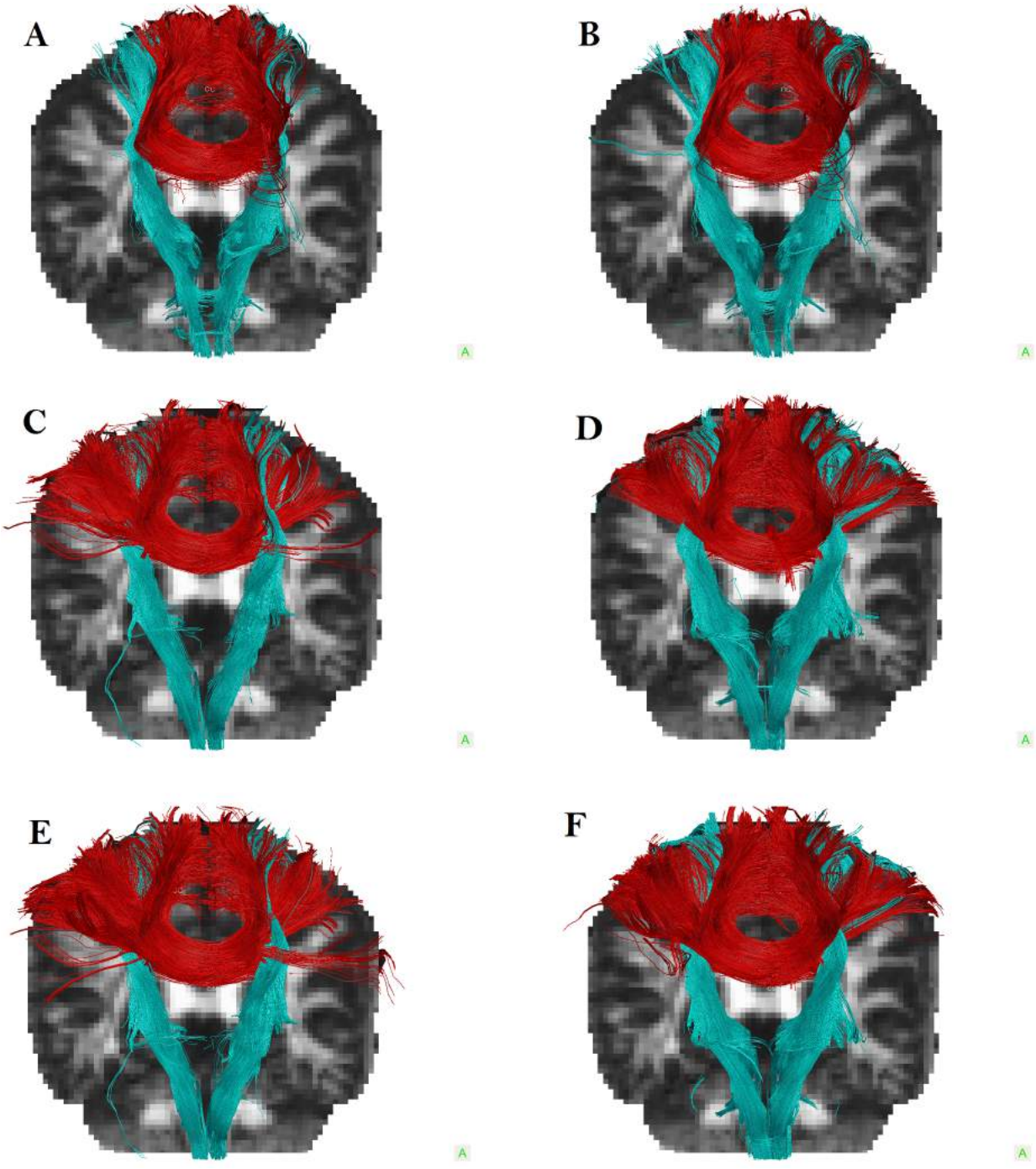

Figure B.4: Tractography reconstructions for subject 4. In cyan the CST tracts, red the CC tracts. In panels A and B, the L-DT and nL-DT reconstructions, respectively; panels B and C show the results for the OLS-KT and OLS-ODF; and panels D and E show the tractography results for CLS-KT and CLS-ODF reconstruction

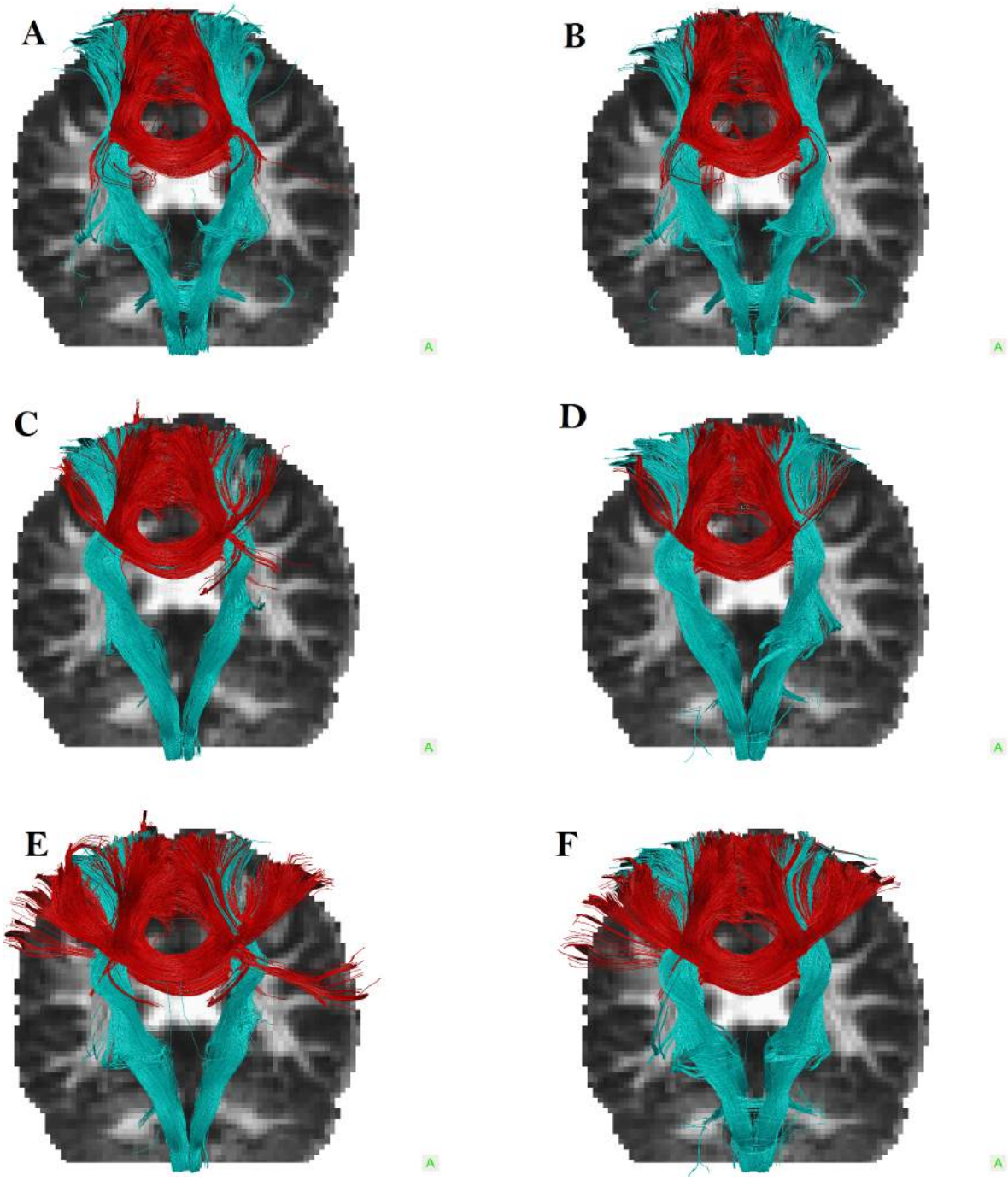

Figure B.5: Tractography reconstructions for subject 5. In cyan the CST tracts, red the CC tracts. In panels A and B, the L-DT and nL-DT reconstructions, respectively; panels B and C show the results for the OLS-KT and OLS-ODF; and panels D and E show the tractography results for CLS-KT and CLS-ODF reconstruction

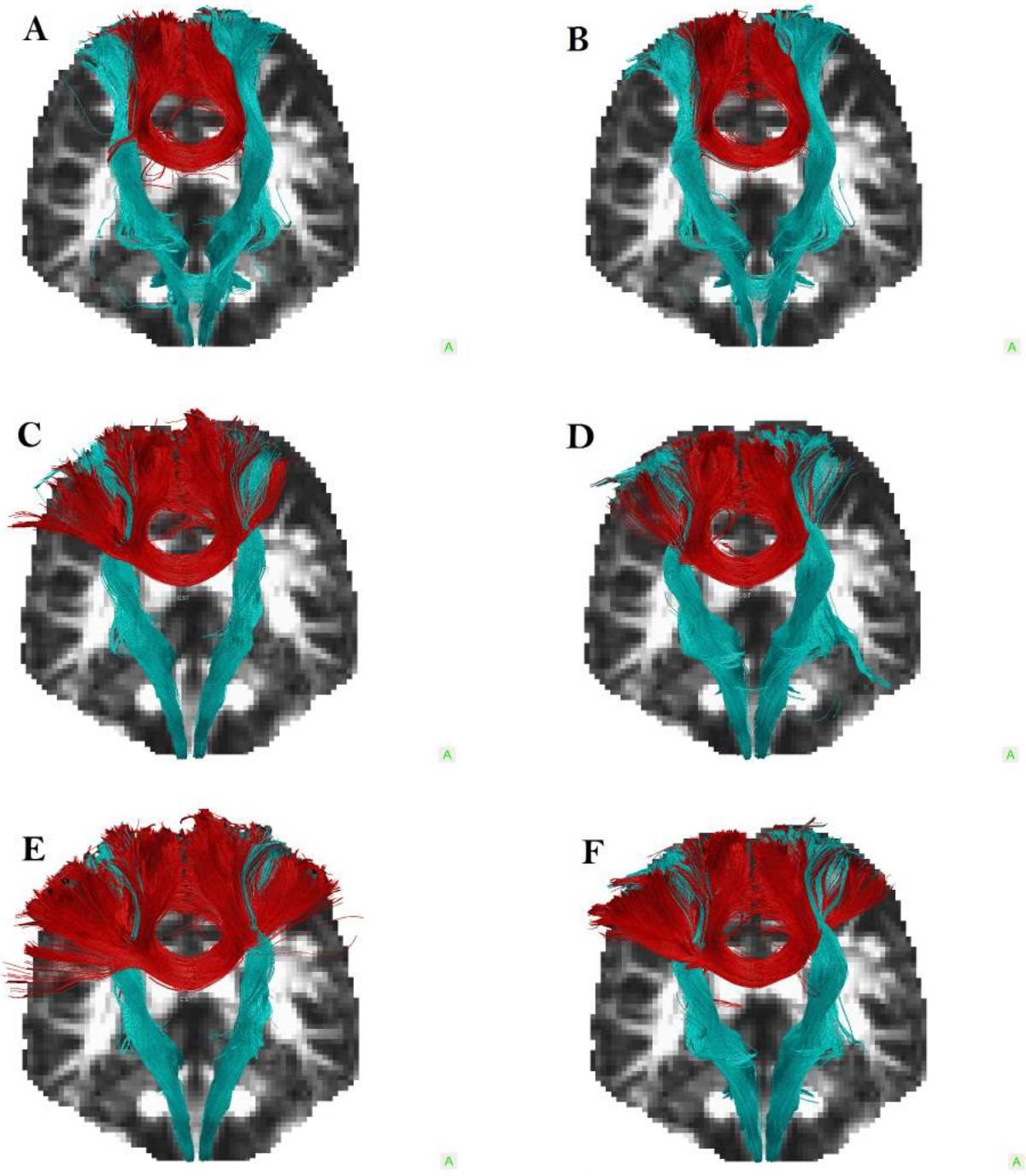

Figure B.6: Tractography reconstructions for subject 6. In cyan the CST tracts, red the CC tracts. In panels A and B, the L-DT and nL-DT reconstructions, respectively; panels B and C show the results for the OLS-KT and OLS-ODF; and panels D and E show the tractography results for CLS-KT and CLS-ODF reconstruction

Appendix

C

Appendix 3 - Bland Altman Plots

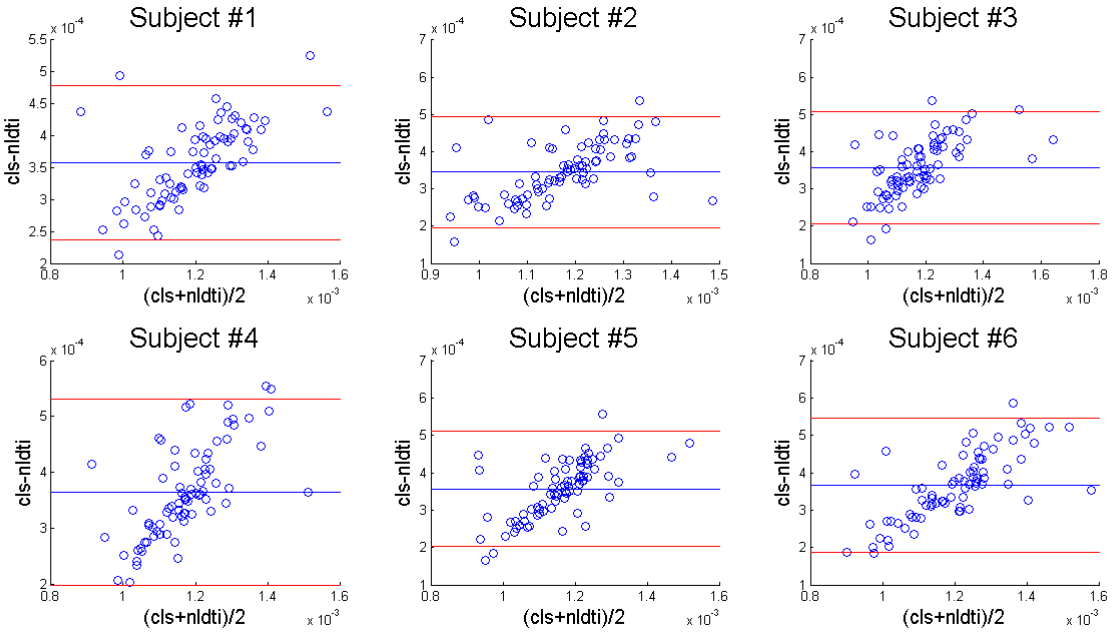

Figure C.1: Bland-Altman plots of AD from CLS-KT and NL-DT. The blue line is the mean of the differences, and the red lines are ±2std. All of the subjects display the same tendency: the difference of the metric increases with the increase of the mean of the metric

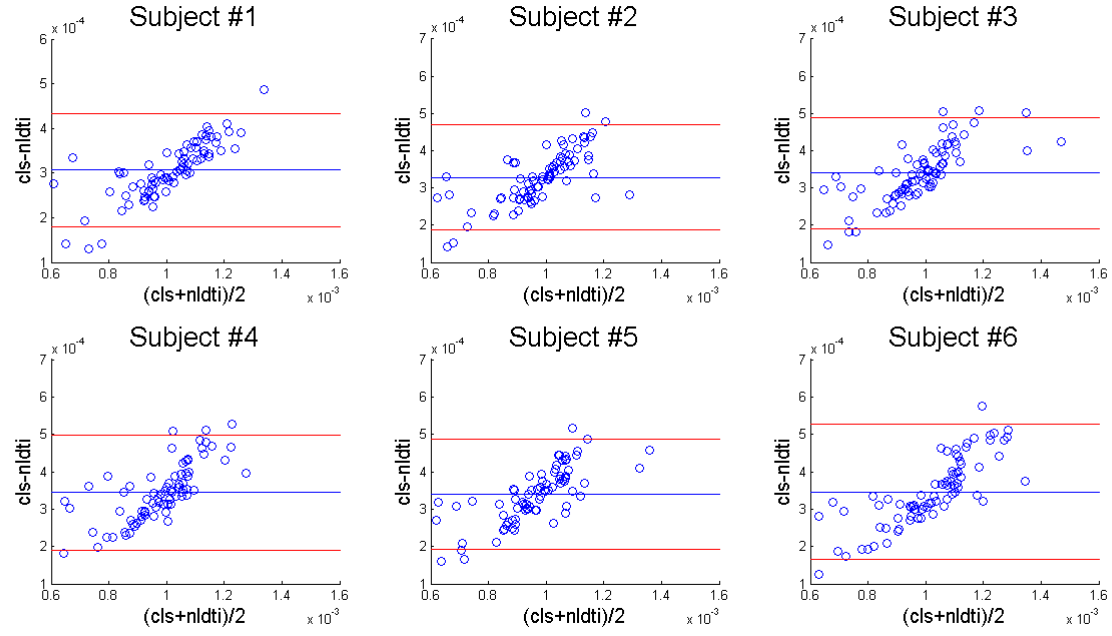

Figure C.2: Bland-Altman plots of RD from CLS-KT and NL-DT. The blue line is the mean of the differences, and the red lines are ±2std. All of the subjects display the same tendency: the difference of the metric increases with the increase of the mean of the metric

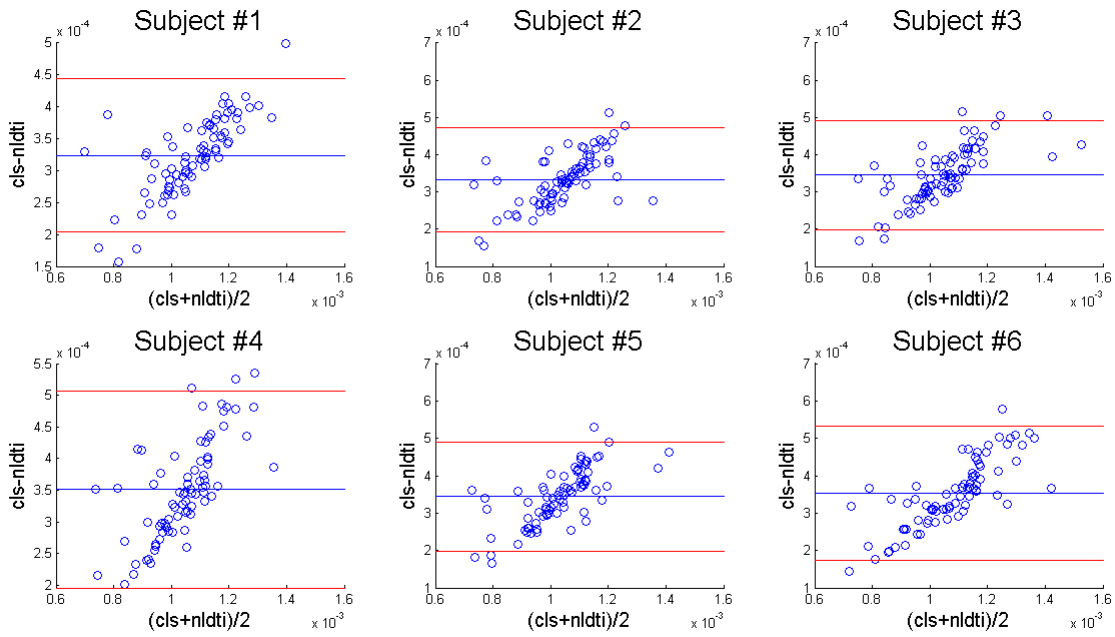

Figure C.3: Bland-Altman plots for MD from CLS-KT and NL-DT. The blue line is the mean of the differences, and the red lines are ±2std. All of the subjects display the same tendency: the difference of the metric increases with the increase of the mean of the metric

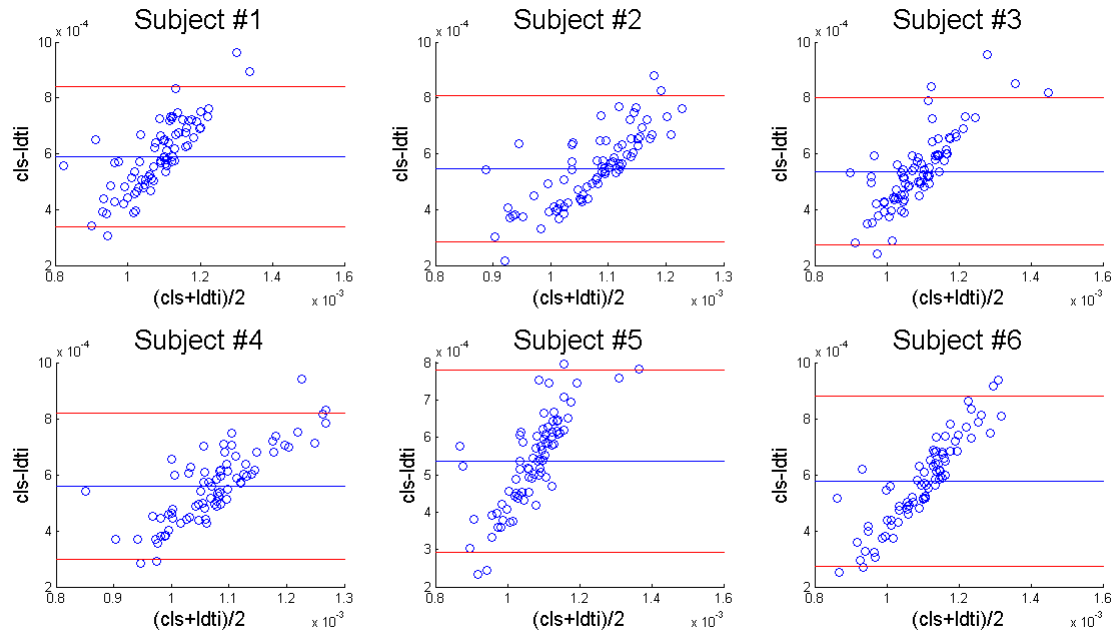

Figure C.4: Bland-Altman plots for AD from CLS-KT and L-DT. The blue line is the mean of the differences, and the red lines are ±2std. All of the subjects display the same tendency: the difference of the metric increases with the increase of the mean of the metric

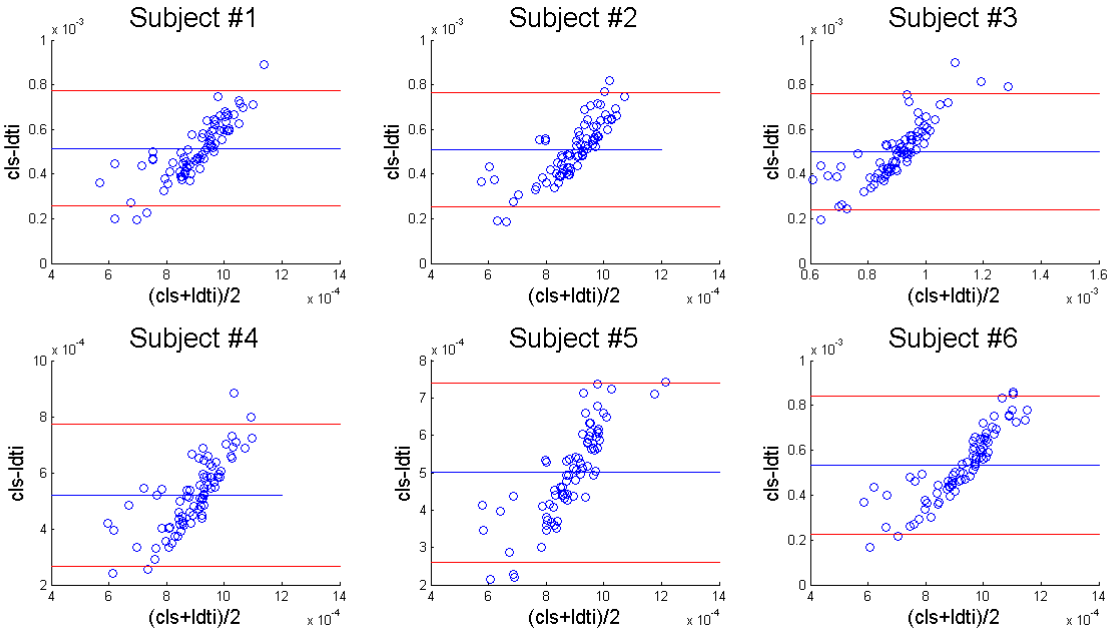

Figure C.5: Bland-Altman plots for RD from CLS-KT and L-DT. The blue line is the mean of the differences, and the red lines are ±2std. All of the subjects display the same tendency: the difference of the metric increases with the increase of the mean of the metric

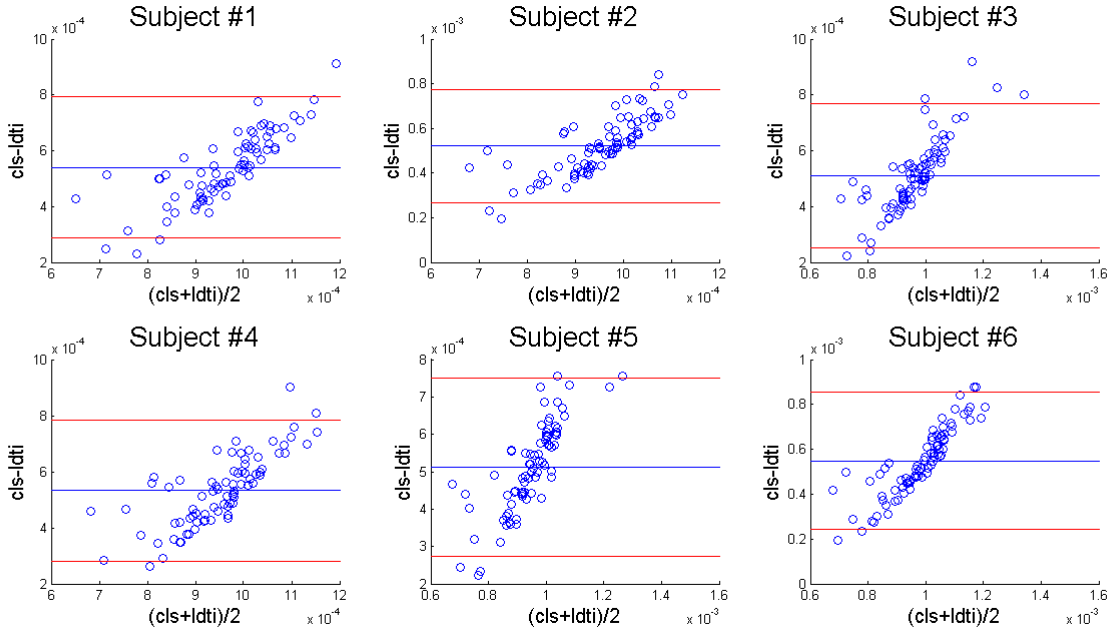

Figure C.6: Bland-Altman plots for MD from CLS-KT and L-DT. The blue line is the mean of the differences, and the red lines are ±2std. All of the subjects display the same tendency: the difference of the metric increases with the increase of the mean of the metric

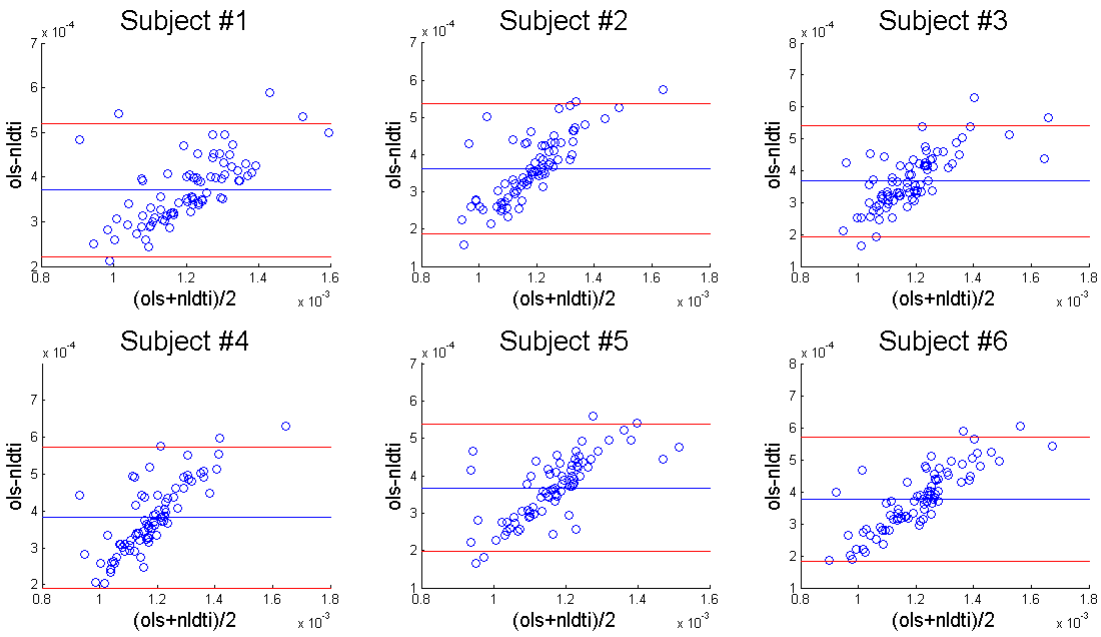

Figure C.7: Bland-Altman plots for AD from OLS-KT and NL-DT. The blue line is the mean of the differences, and the red lines are ±2std. All of the subjects display the same tendency: the difference of the metric increases with the increase of the mean of the metric

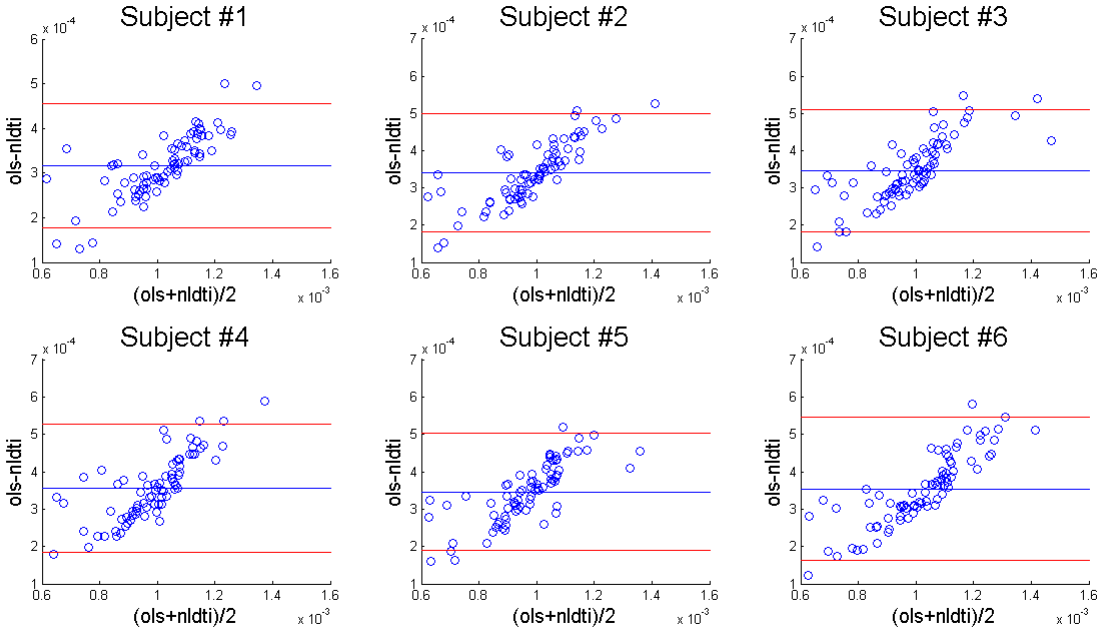

Figure C.8: Bland-Altman plots for RD from OLS-KT and NL-DT. The blue line is the mean of the differences, and the red lines are ±2std. All of the subjects display the same tendency: the difference of the metric increases with the increase of the mean of the metric

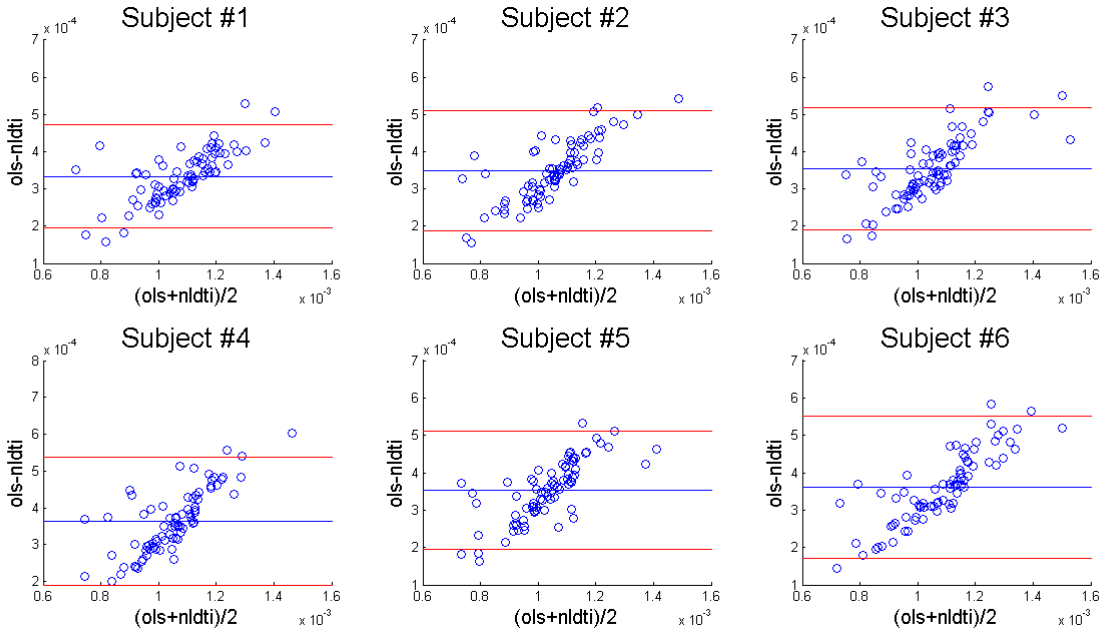

Figure C.9: Bland-Altman plots for MD from OLS-KT and NL-DT. The blue line is the mean of the differences, and the red lines are ±2std. All of the subjects display the same tendency: the difference of the metric increases with the increase of the mean of the metric

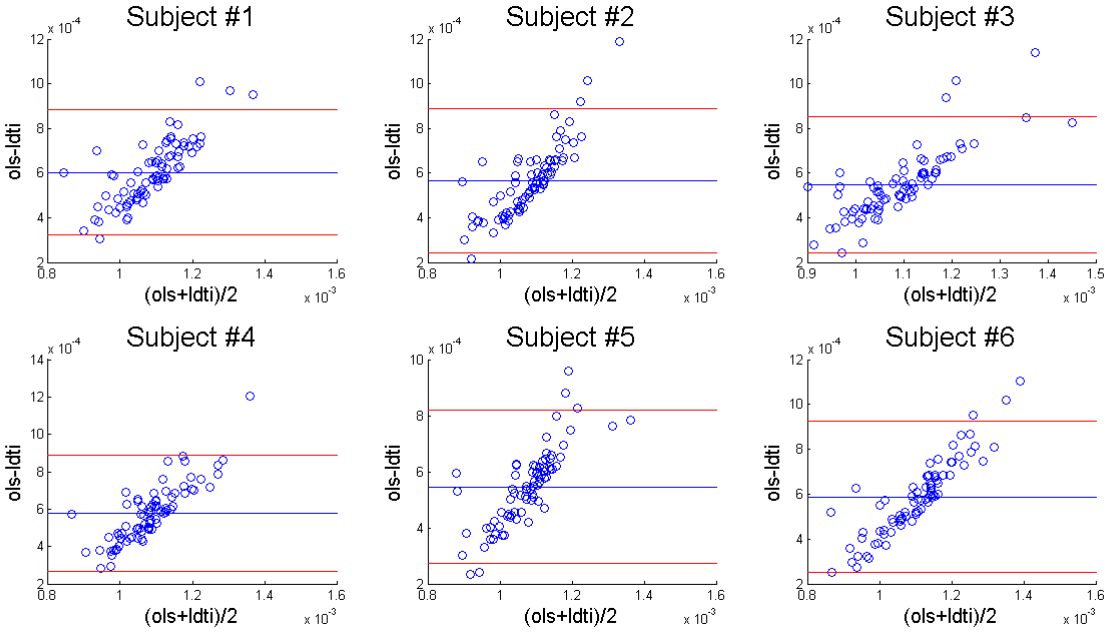

Figure C.10: Bland-Altman plots for AD from OLS-KT and L-DT. The blue line is the mean of the differences, and the red lines are ±2std. All of the subjects display the same tendency: the difference of the metric increases with the increase of the mean of the metric

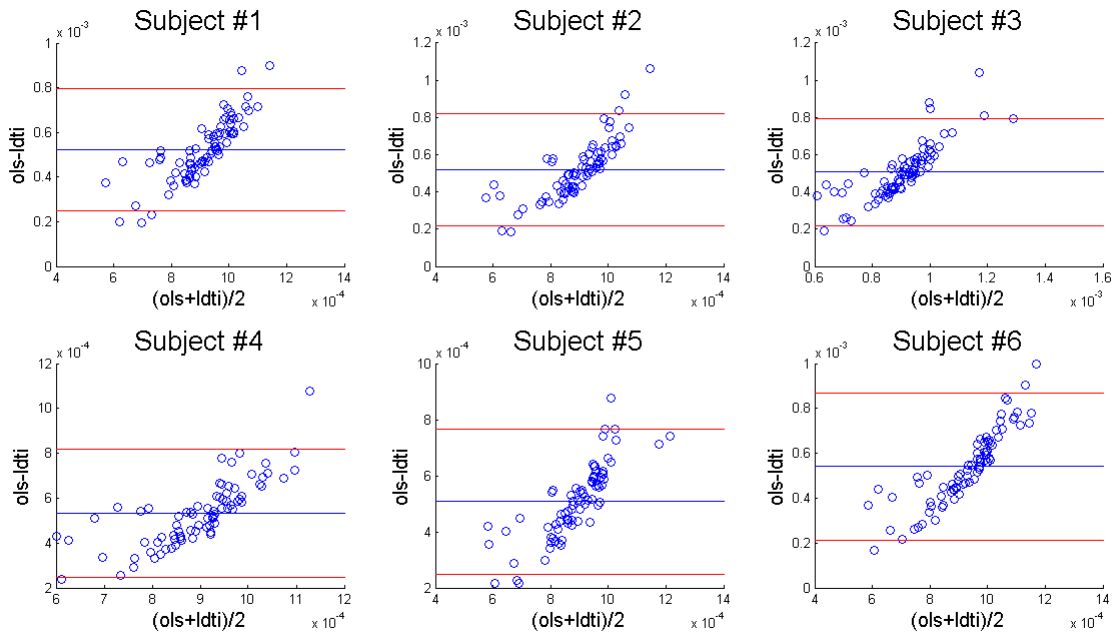

Figure C.11: Bland-Altman plots for RD from OLS-KT and L-DT. The blue line is the mean of the differences, and the red lines are ±2std. All of the subjects display the same tendency: the difference of the metric increases with the increase of the mean of the metric

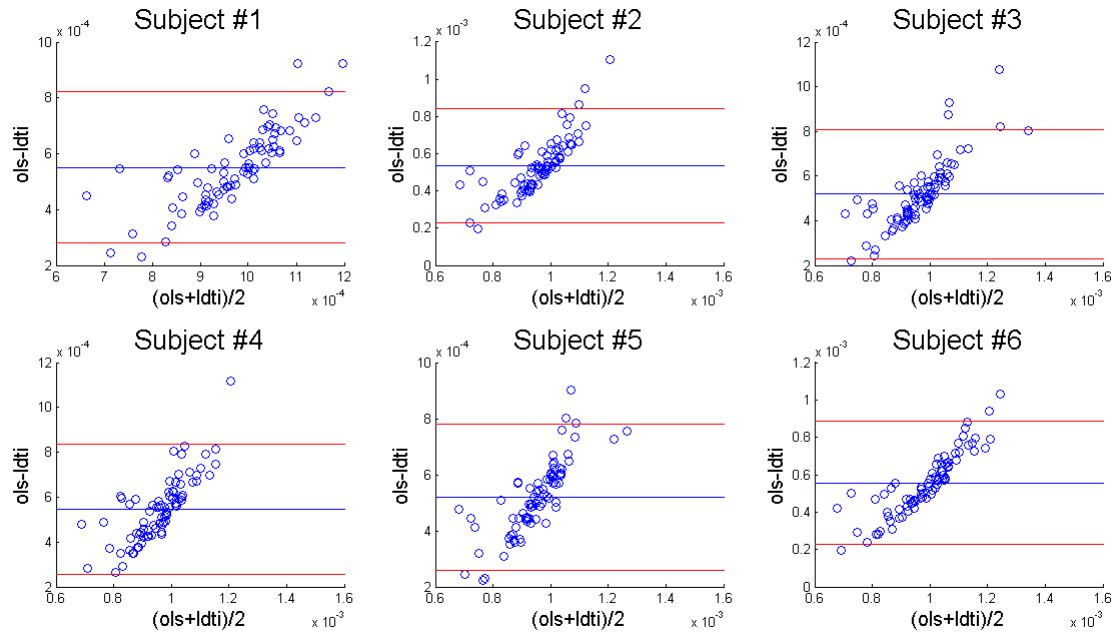

Figure C.12: Bland-Altman plots for MD from OLS-KT and L-DT. The blue line is the mean of the differences, and the red lines are ±2std. All of the subjects display the same tendency: the difference of the metric increases with the increase of the mean of the metric